ORNL/TM-2019/1341

Oxidation of Matrix Material in Helium with Varied Moisture Content

Tyler J. Gerczak
Cristian Contescu
Jo Jo Lee
Robert Mee
Austin Schumacher
John Stempien
Michael Trammell

November 2019

OAK RIDGE NATIONAL LABORATORY
MANAGED BY UT-BATTELLE FOR THE US DEPARTMENT OF ENERGY

ORNL/TM-2019/1341

Reactor and Nuclear Systems Division

OXIDATION OF MATRIX MATERIAL IN HELIUM WITH VARIED MOISTURE CONTENT

Tyler J. Gerczak
Cristian Contescu
Jo Jo Lee
Robert Mee
Austin Schumacher
John Stempien
Michael Trammell

November 2019

Prepared by
OAK RIDGE NATIONAL LABORATORY
Oak Ridge, TN 37831-6283
managed by
UT-BATTELLE, LLC
for the
US DEPARTMENT OF ENERGY
under contract DE-AC05-00OR22725

CONTENTS

LIST OF FIGURES

LIST OF TABLES

ACRONYMS

AGR	Advanced Gas Reactor Fuel Development and Qualification Program
BLH	Boltzmann Langmuir-Hinshelwood (LH)
CVD	chemical vapor deposition
DOE	US Department of Energy
HTGR	high-temperature gas-cooled reactor
HTM	high-temperature module
LH	Langmuir-Hinshelwood
ORNL	Oak Ridge National Laboratory
SATS	Severe Accident Test Station
SiC	silicon carbide (TRISO layer)
SSE	sum of squared errors
TRISO	tristructural-isotropic (coated particles)
UHP-He	ultrahigh purity He
WL	weight loss

ACKNOWLEDGMENTS

This work was supported by the US Department of Energy's Office of Nuclear Energy Advanced Reactor Technologies as part of the Advanced Gas-Cooled Reactor Fuel Qualification and Development Program. Significant support for this work was provided by Victoria Cox, Tom Geer, Michael Howell, and Daniel Newberry.

ABSTRACT

Exploration of the oxidation behavior of matrix material from tristructural-isotropic (TRISO) coated particle fuel elements in moisture environments provides critical data needed to predict the material's response during off-normal accident scenarios. Near-representative, matrix-only samples were fabricated to facilitate oxidation testing in varied moisture concentrations. Oxidation testing was completed over a range of temperatures and oxidizing environments to obtain the relevant oxidation kinetics parameters and empirical oxidation rates necessary to better predict and understand matrix oxidation behavior at relevant conditions. The acquired oxidations rates were fit to established models for steam oxidation of nuclear graphite, and data were acquired following an established process. The data showed good agreement over conditions typical of the kinetic regime, and they showed a departure from the kinetic model fit at elevated temperatures and steam partial pressures in helium carrier gas. The departure was confirmed to be due to the experimental conditions being beyond the kinetic regime based on destructive analysis.

1. INTRODUCTION

High-temperature gas-cooled reactors (HTGRs) traditionally use tristructural-isotropic (TRISO) coated particle fuel compacted in a graphite and carbonized resin matrix to produce a fuel element. The matrix-material surrounds the fuel particles and provides structural integrity and protection to the TRISO fuel particles. Accident scenarios in HTGRs include air and moisture ingress events at high temperatures. The likelihood of such accidents may vary among HTGR designs such that air or moisture-ingress events are design-basis accidents for one design but beyond design-basis for another design. The US Department of Energy (DOE) Advanced Gas Reactor Fuel Qualification and Development Program (AGR) initiated an experimental effort to better understand the oxidation response of each component in such events. By testing each component (matrix-only TRISO particles) separately, the oxidation behavior can be isolated, measured, and subsequently leveraged in fuel performance models to better predict performance.

Steam ingress events ultimately lead to acute corrosion of graphitic materials in the HTGR core. The extent of oxidation of graphitic materials will vary based on many parameters including, but not limited to, location in the core, duration of the accident, and the quantity of oxidant to infiltrate the system. In prismatic HTGRs, cylindrical fuel elements (called compacts) are contained in channels in large blocks of graphite. Separate channels in these blocks carry the helium coolant. These blocks will naturally act to shield the fuel from oxidants. Pebble bed HTGRs consist of a bed of spherical fuel elements where the coolant flows through the bed and directly around each pebble. Many fuel pebble designs feature an un-fueled zone of matrix that protects the TRISO particles in the pebbles. Pebble bed reactors may also have large graphite core structures such as neutron reflectors, that would also consume oxidants. If oxidants were able to reach the fuel elements, oxidation of the fuel elements may lead to radionuclides being released into the coolant and an increased potential for TRISO particle degradation. Water ingress events could be caused by a moderate-sized break of a steam generator tube, steam leakage in the primary coolant system, and depressurization of the primary coolant system [1]. These events are expected to yield scenarios in which the fuel elements are exposed to variable steam partial pressures (P_{H2O}) and temperatures, depending on the nature of the event. Table 1 describes generic conditions that may be experienced during the varied accident conditions [1–7]. These conditions form the basis for the oxidation testing conditions discussed here-in.

Table 1. Relevant conditions for a steam ingress events [1–7].

Peak fuel temperatures (°C)	1,000–1,630
H_2O partial pressure (kPa)	≤ 2 (for tens of hours) ≤ 400 (for up to several hours)
Time to reach peak fuel temperature (h)	~100

The oxidation behavior of the matrix material in steam environments has not been well studied; however, the oxidation performance in air has been analyzed between 500–1,600 °C [8,9]. The oxidation behavior for different grades of nuclear graphite in steam conditions relevant to chronic oxidation of HTGR internal components has been well established [10–12]. These tests focused primarily on the kinetic oxidation regimes ($T < 1{,}000$ °C, $0.01 \leq P_{H2O} \leq 3$ kPa) and conditions relevant to chronic oxidation to obtain oxidation kinetic parameters. These tests were identified to meet the kinetic regime and conditions relevant to chronic oxidation. These conditions are at lower temperatures and partial pressures than the peak values expected for acute moisture ingress accidents relevant. Additionally, the matrix material is a composite of natural and synthetic graphite flake and carbonized resin binder as such existing data on nuclear graphite stream oxidation may not translate directly. This defines a need to directly analyze the oxidation performance of matrix material. The experimental approaches developed for nuclear-grade graphite steam oxidation can be leveraged to investigate steam oxidation of matrix materials.

The goal of this effort is to acquire the kinetic parameters for steam oxidation of near-representative matrix-only material and to obtain empirical oxidation rates at conditions relevant to accident scenarios. The oxidation of graphitic materials follows the global reaction presented in Equation 1.

$$\boldsymbol{C_{solid} + H_2O_{vapor} = CO_{gas} + H_{2\,gas}} \quad (1)$$

Based on the global equation, the presence of the reaction products (CO_{gas} *and* $H_{2\,gas}$) will shift the equilibrium and influence the overall oxidation rate [13]. In particular, hydrogen will suppress the reaction by occupying surface sites on the graphite surface [8,14]. Therefore, the influence of the partial pressure of hydrogen (P_{H2}) must be considered when analyzing the oxidation behavior in a steam environment. The requirement for analyzing varying P_{H2} to determine the kinetic parameters is discussed in more detail in Section 2.3.1.

While the composite matrix material likely responds differently to oxidation compared to nuclear grade graphite, the underlying oxidation behavior likely translate based on the similarity in composition. The characteristics of the oxidation of graphite can be illustrated in three different regimes showing the observed Arrhenius temperature dependence. The specifics of each regime are described in detail by Kane et al. [15]. At low temperatures, oxidation behavior is controlled by the rate of the chemical reaction. This regime is considered the *kinetic regime*, and oxidation occurs uniformly throughout the material. At higher temperatures, oxidation is impacted by diffusion of the oxidant and the rate of the chemical reaction. This regime is described as the *transition regime*, and it is highlighted by nonuniform oxidation. Specifically, the oxidation is more pronounced at the surface, with clear penetration into the bulk. At even higher temperatures, the oxidation is controlled by the rate of oxidant diffusion to the surface of the samples. The oxidation reaction is confined to the exposed surface, and the reaction leads to a reduction in surface area; this regime is defined here as the *diffusion-controlled regime*. Figure 1 shows a schematic of the oxidant profiles for each regime to illustrate the different oxidation scenarios [15]. Exploration of test conditions in the *kinetic regime* are targeted for the determination of the kinetic

parameters in this study, while the exploration of temperatures and steam partial pressures relevant to accident conditions are expected to probe the *transition regime* and/or *diffusion-controlled regime.*

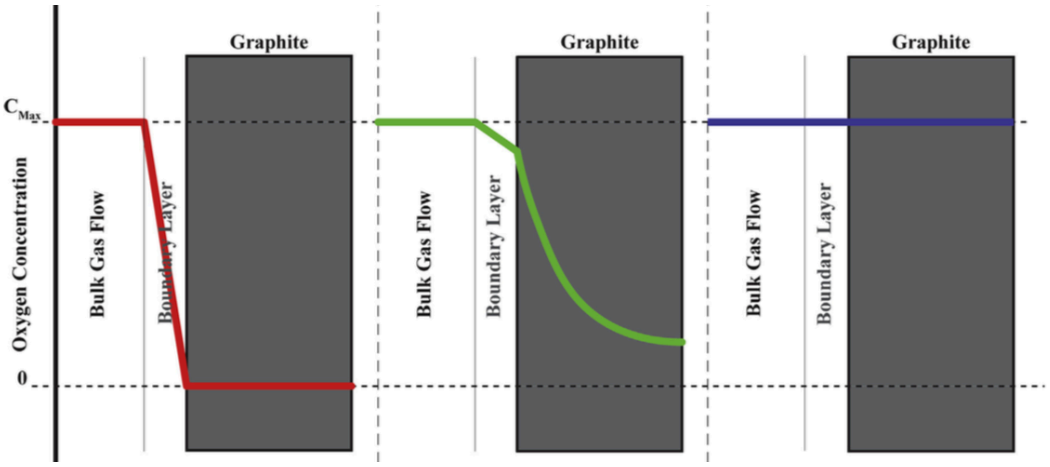

Figure 1. Schematic of oxidant profiles for each oxidation regime; (left) *diffusion-controlled regime,* (center) *transition regime, and* (right) *kinetic regime* (reproduced from Kane et al. [15]).

In 2012, an effort at Oak Ridge National Laboratory (ORNL) to measure the steam oxidation kinetics of various nuclear-grade graphites was initiated [12,13,16–18]. This past effort serves as a template for analyzing the oxidation kinetics of matrix-only material in varied moisture environments, and it includes measured oxidation rates under various P_{H2O} and P_{H2}. This testing approach focused on determining the relevant kinetic parameters based on an established model, Langmuir-Hinshelwood (LH) [19], and on a new model, the Boltzmann-enhanced Langmuir-Hinshelwood (BLH) model, which accounts for the temperature dependence of the reaction order [20]. The general test matrix for these studies was adopted for the analysis of matrix-only samples. The oxidation behavior at near-accident conditions was pursued to obtain empirical rates so that oxidation behavior at extreme conditions can be predicted better, the nature of the oxidation response can be better understood. An existing high-temperature steam exposure system, the Severe Accident Test Station (SATS), was leveraged to study this behavior. This system limited the conditions which could be obtained through testing in the that the system operated a nominally atmospheric pressure.

2. EXPERIMENTAL APPROACH

2.1 FABRICATION OF MATRIX-ONLY SAMPLES

Samples for matrix oxidation testing were fabricated to meet the specification of matrix material from the AGR-5/6/7 irradiation experiment [21]. The matrix precursor materials were acquired from BWXT and consisted of a blend of natural graphite, synthetic graphite, resin binder, and hardening agent. The matrix blend used was consistent with the raw materials and the materials ratios representative of AGR-5/6/7 matrix. This matrix blend was compacted using procedures defined through the AGR program's laboratory-scale compacting efforts to produce matrix-only samples for oxidation testing.

Existing dies were utilized to produce cylindrical samples. A thin disk shape was developed for the test samples to limit density variation across the thickness of the specimen and to maintain the appropriate ratio of surface area to volume of approximately 1:1.1 to minimize volume effects during oxidation testing [8]. The selected disk geometry was approximately 2.58 mm thick with a 12.1 mm diameter. The samples were produced to meet the AGR-5/6/7 fuel specification for matrix density, with the primary

criteria being a geometric density ≥ 1.65 g/cm^3 [21], while targeting a density of 1.75 g/cm^3 to represent AGR-5/6/7 [22].

The process to produce matrix samples included multiple steps. The fabrication process included producing a sample charge, pressing a green compact, performing sample carbonization, and conducting a final heat treatment to drive out impurities. The sample ID was tracked throughout the fabrication process, and measurements were taken at interim stages so possible variations in sample outcomes and initial density could be noted. The matrix-only samples are expected to have a similar chemical composition but a different microstructure than the AGR-5/6/7 fuel compacts. The absence of fuel particles in the matrix-only samples is expected to impact the overall orientation of the graphite flake and the local variation in matrix density. The expected texture differences likely do not impact oxidation in the kinetic regime, where oxidation occurs uniformly, but it may influence the observed oxidation rate at diffusion-dependent conditions beyond the *kinetic regime* [15]. While carbonization and heat treatment conditions were the same for the matrix-only samples and the fuel compacts, the equipment used was different, and the pressing procedure to make the matrix-only samples was optimized for the oxidation test samples.

Pressing was initiated by first weighing ~0.62 g of the graphite/resin blend and then hand-pressing the material to produce a die charge. This charge was then lightly ground with SiC-grit sanding paper to achieve a sample with a mass of ~0.58 g. This step helped to ensure that the mass of the samples was consistent. A green compact was produced by hot pressing the charge in a die heated at 155 °C and subjecting it to 1.3 kN for 60 s using the Promess automated servo-driven mechanical press shown in Figure 2. The green compacts were then subjected to a carbonization step to finish curing and to carbonize the resin binder. This thermal exposure was performed in a Lindberg/Blue® tube furnace. The approximate carbonization schedule is shown in Table 2 and follows the same temperature profile as those used to produce fuel compacts [23]. After carbonization, the samples were subjected to a final high-temperature heat treatment at 1800 °C for one hour, increasing 20 °C/min, ramping from 20 up to 1,800 °C. The heat treatment was performed under vacuum, with a starting vacuum of < ~100 Pa in a Thermal Technology, Inc. ASTRO furnace. This step drives out impurities present in the sample and yields the final geometry and density. Minimal geometry variation was observed after the high-temperature heat treatment compared to the post-carbonization sample.

Figure 2. Matrix pressing assembly showing temperature-controlled heated die with automated Promess servo press.

Table 2. Matrix carbonization schedule, all values approximate.

Step (°C)	Ramp rate (°C/min)	Step duration (min)
20 → 140	4	30
140 → 220	1	80
220 → 330	1	80
330 → 420	1	180
420 → 560	1	170
560 → 610	2	25
610 → 690	4	20
690 → 900	6	35
900 → 900	hold temperature	30
900 → 20	20	45

The final heat-treated samples were subjected to dimensional inspection and density calculation according to AGR-CHAR-DAM-39, a procedure previously developed procedure for matrix-only compact dimension and density measurements from the AGR program. The ultimate length of the matrix samples did not allow for the diameter to be measured at multiple axial positions according to the procedure. Therefore, the procedure was modified. In particular, the diameter measurement was taken at the middle of the sample as opposed to the three positions used for standard cylindrical compacts, which were each one inch long. Three unique measurements around the circumference of the sample (~60° increments) were taken in lieu of measurements at different axial positions. Sample dimensions and mass were measured on calibrated equipment according to applicable NQA-1 standards. This included validation of balances and calipers prior to obtaining measurements through the use of certified mass standards and gauge blocks.

An acceptance criterion was established based on a visual standard and the measured density. After the samples were prepared, their outer surfaces were visually inspected for surface irregularities. Samples with surface fissures and other gross surface features were rejected. The presence of surface fissures was an expected defect based on past experience with full-sized blank (unfueled) compacts using the AGR-5/6/7 matrix formulation and methods [23]. Examples of surface fissures prompting rejection are shown in Figure 3. Surface fissures are not expected to influence oxidation behavior in the *kinetic regime* due the uniform oxidation behavior, however, the presence of fissures may impact oxidation in the surface sensitive regimes beyond the *kinetic regime*. Samples with measured densities within two standard deviations (σ) of the mean were considered acceptable. Figure 4 shows the inspection results for the 300 samples produced, presenting the measured density and mean and the standard deviation band for the visually accepted samples. The mean density of the final sample set after visual acceptance was 1.760 g/cm^3 with a standard deviation of 0.025 g/cm^3. Samples within a range of 2σ were accepted for testing (1.711–1.810 g/cm^3). The majority of samples were rejected based on visual inspection (surface fissures), with only two samples rejected due to density measurements alone. The matrix-only acceptance rate was ~37% which was expected based on previous experience [23]. Appendix A lists the measured properties of the as-fabricated samples and the associated acceptance criteria.

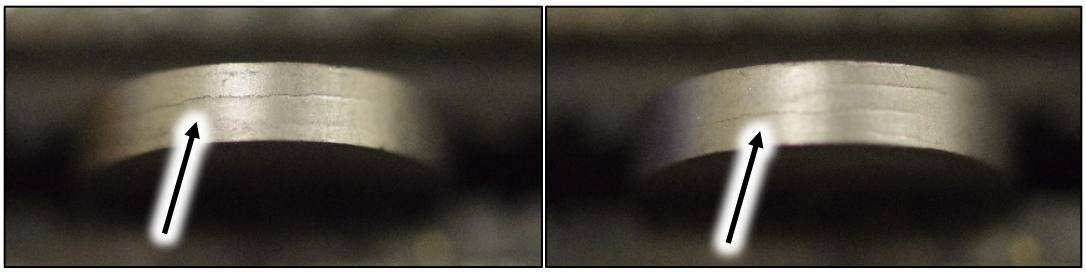

Figure 3. Examples of surface fissures prompting rejection in matrix-only samples.

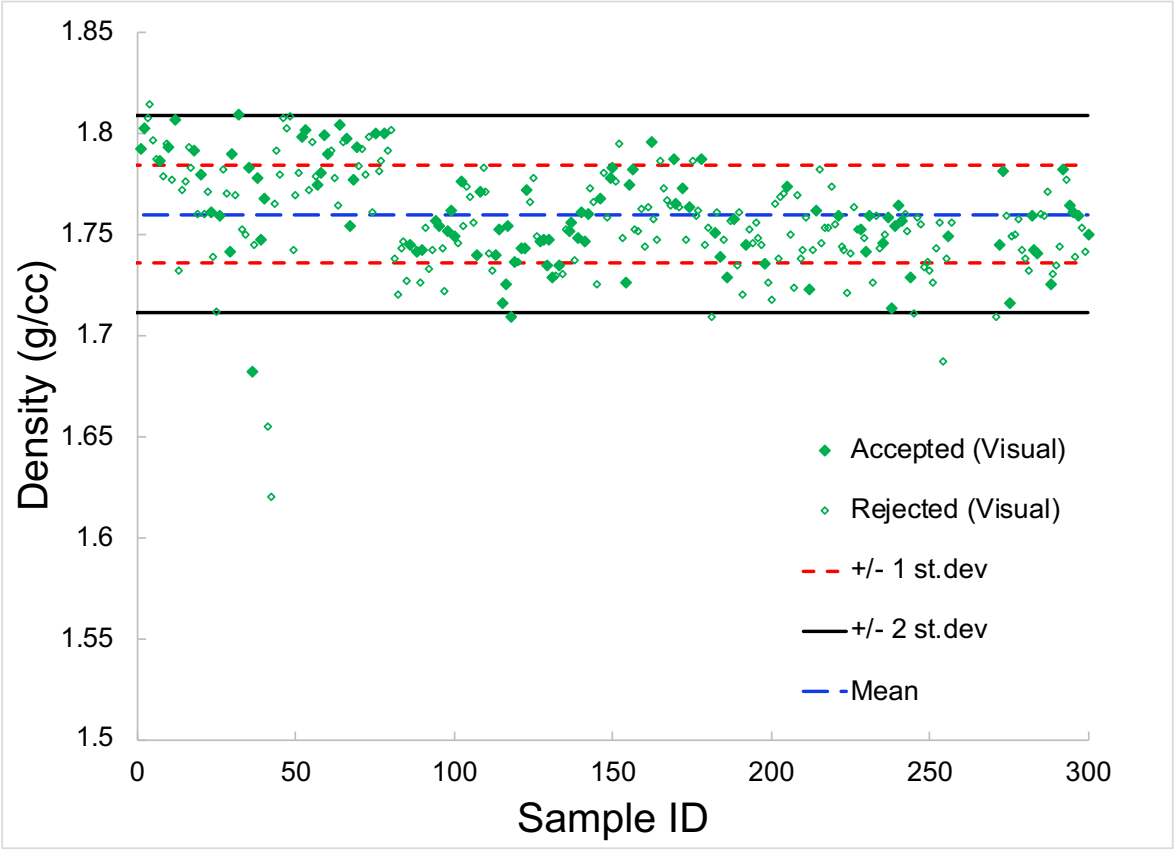

Figure 4. Measured density for matrix-only samples accepted and rejected based on visual criteria. Displayed mean and standard deviation bands are associated with visually accepted samples only.

2.2 OXIDATION SYSTEMS

2.2.1 Testing System for Oxidation Kinetics Evaluation

The oxidation behavior to obtain kinetic parameters was examined using a dual symmetrical thermogravimetric analyzer TAG 16/18 (Setaram, France). This system has been described in detail in the literature and was designed for oxidation kinetic measurements of nuclear graphite [12,13,16–18]. The experience obtained from steam oxidation testing of nuclear-grade graphite was leveraged to initiate and test oxidation behavior of the matrix-only material. Figure 5 shows a schematic and image of the experimental system.

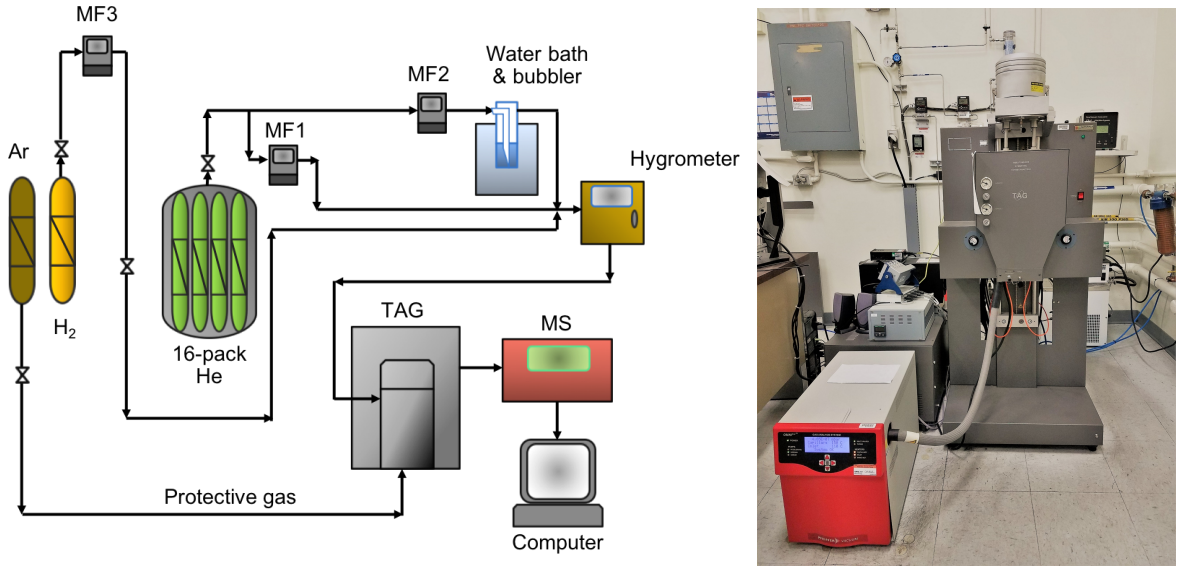

Figure 5. Schematic and image of the dual symmetrical thermogravimetric analyzer—TAG 16/18—used in this study.

The system was operated at total flow rates of 1.5 L/min. The oxidant was delivered to the sample via ultrahigh purity helium (UHP-He) (> 99.999 vol. %). The partial pressures of water vapor (P_{H2O}) and hydrogen (P_{H2}) in the UHP-He carrier gas were controlled for each exposure condition. The range of possible P_{H2O} was 3–1000 Pa, and the range in P_{H2} was 0–100 Pa. The temperature regime analyzed was 800–1200 °C. Table 3 shows the targeted test conditions for each exposure. As previously described, this test matrix was based on tests performed to study the oxidation kinetics of nuclear-grade graphite [12,13,16–18]. However, this test matrix is skewed toward higher P_{H2O} to better reflect accident conditions and to link to the separate high-temperature oxidation tests run as part of this program.

Table 3. Test matrix for oxidation kinetics evaluation in varied moisture environments (P_{H2O}, P_{H2} in UHP-He).

Gas compositions	P_{H2O} (Pa)	5	20	50	100	150	200	250	300	500	1000
P_{H2} (Pa)	0 (2×)*		✓		✓		✓		✓	✓	✓
	25		✓		✓		✓		✓	✓	
	100		✓		✓		✓		✓	✓	

*2× indicates the P_{H2O} condition was repeated

Multiple temperatures were analyzed for each combination of P_{H2O} and P_{H2}. Oxidation rates were determined by weight loss measurements at constant temperature over holds of at least 3 h. Temperature ramps began at the lowest temperature first, 800 °C, with 50 °C incremental steps up to 1,200 °C. Longer exposure times >5 h were used for lower temperatures due to the expected limited oxidation at lower temperatures (<900 °C) relative to the higher temperature conditions. The 1,200 °C test condition was not completed for all runs, as it was included after some initial tests had already been run to provide a link to the high-temperature empirical oxidation testing. Figure 6 shows the temperature profile for a typical oxidation kinetics testing run. The initial ramp to 1,200 °C with 0.5 h hold under vacuum and 1 h outgas serves to drive off residual moisture and other volatile species on the surface of the sample before testing. A new sample was used for each condition, that is, each combination of P_{H2O} and P_{H2}. Figure 7 shows examples of the measured weight loss for P_{H2O} =100 Pa and P_{H2} = 0 Pa, as well as and P_{H2O} =100 Pa and

P_{H2} = 25 Pa. The comparison illustrates the suppression of weight loss with the addition of H_2 to the system, which is expected due the global oxidation reaction shown in Equation 1 [13].

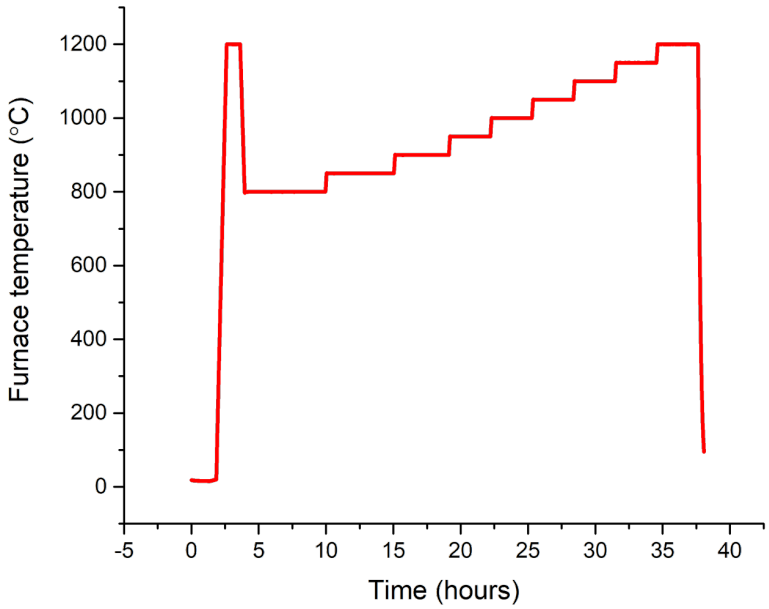

Figure 6. Typical temperature profile for oxidation testing in the TAG system.

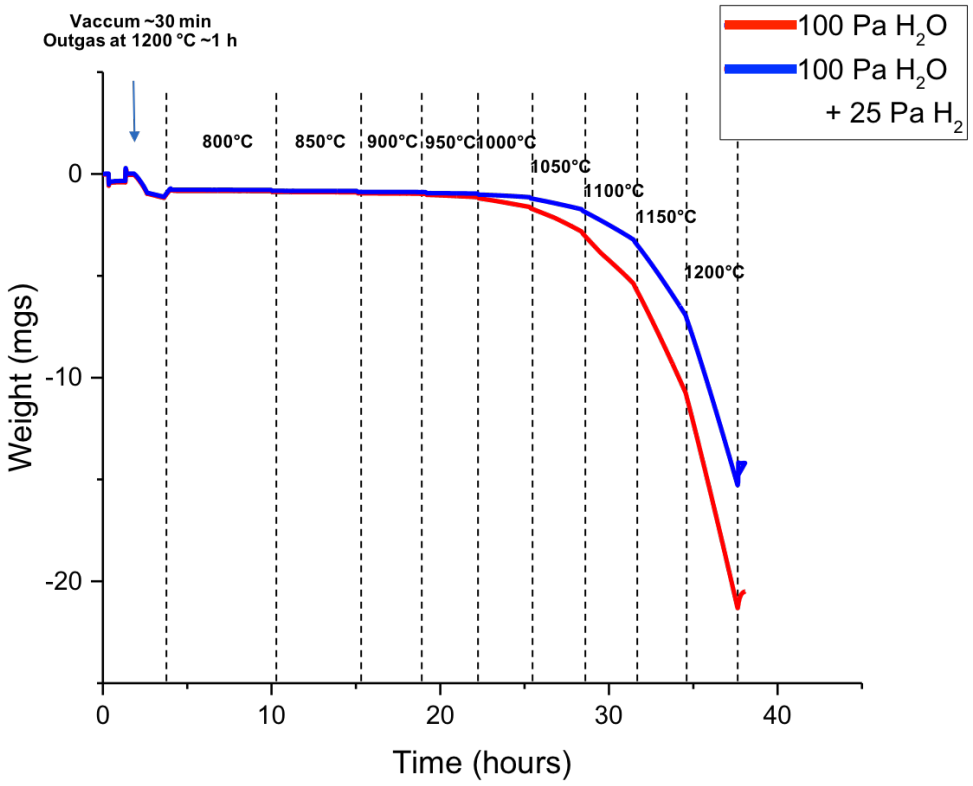

Figure 7. Example of weight loss measurements for oxidation testing over 800–1,200 °C at P_{H2O} =100 Pa and P_{H2} = 0 Pa, as well as P_{H2O} =100 Pa and P_{H2} = 25 Pa.

2.2.2 Testing System for High-Temperature Empirical Oxidation

Oxidation tests were conducted at temperatures higher than those in the oxidation kinetics evaluation described in the previous section, and they required a different testing system due to limitations of the TAG. The high-temperature empirical oxidation tests serve to mimic most extreme temperatures and moisture partial pressures in the reactor core. For short duration accidents or cases where sufficient core graphite exists to shield the fuel from moisture, the fuel itself may not see such high moisture partial pressures. The high-temperature module (HTM) of the SATS was identified as an appropriate test system (Figure 8). The furnace is capable of operation above 1,600 °C and up to 100% steam conditions. The standard system is described in detail by Terrani et al. [24].

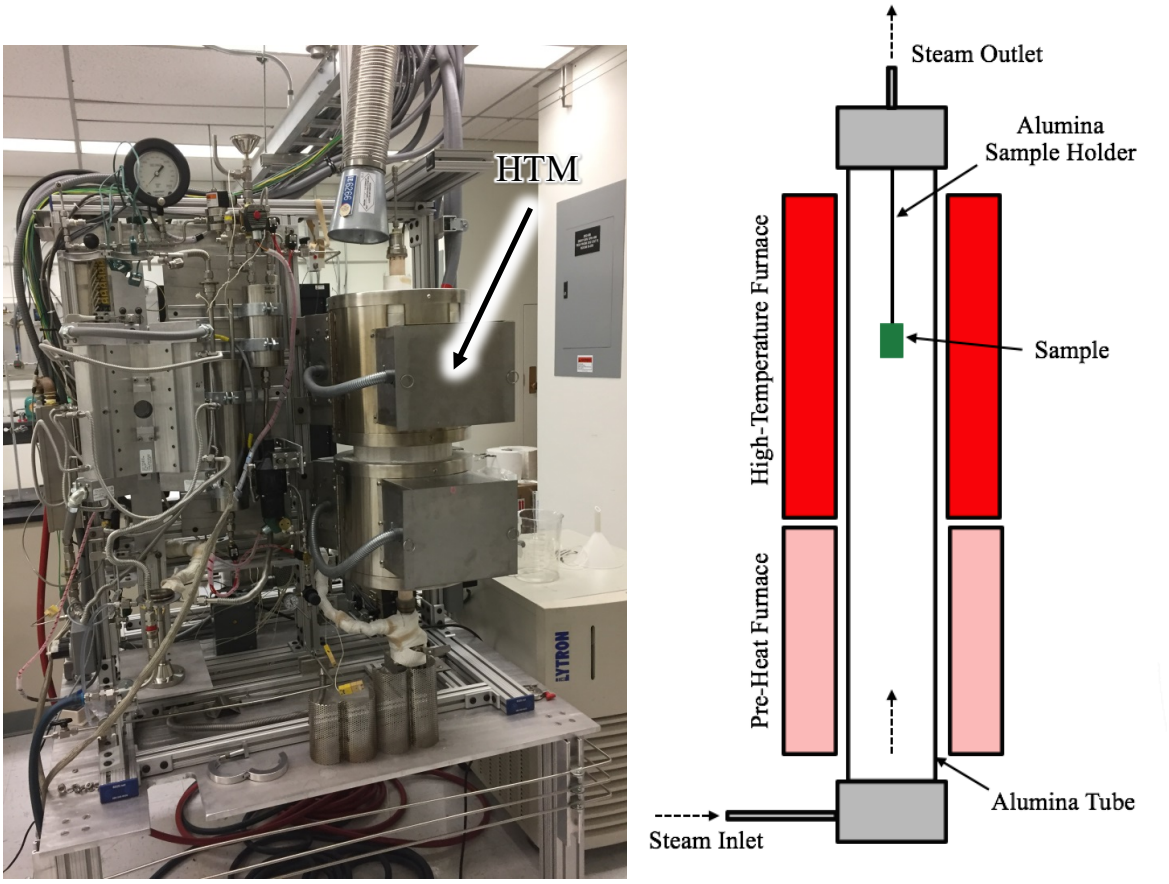

Figure 8. SATS system for high-temperature empirical oxidation testing (schematic adapted from Terrani et al. [24]).

The oxidation environment was controlled by continuously injecting water into a steam injector using a peristaltic pump. The water vapor was carried via UHP-He gas into the furnace chamber at 500 cc/min. All inlet lines were wrapped with heat tape to avoid condensation. Upon entering the furnace, the steam and carrier gas enters a lower furnace chamber where the gas is preheated to 800 °C. The gas then enters the HT-module where the oxidation sample resides in a constant temperature regime up to 1600 °C. The matrix-only oxidation samples were suspended in the constant temperature zone of the HT-module on an alumina sample holder. A 3/16" diameter hole was drilled in each sample prior to testing (Figure 9c). The samples were hung on a chemically vapor deposited silicon carbide (CVD-SiC) rod positioned between two prongs on the alumina sample holder (Figure 9d). The gas exits the system via a gas outlet line which was wrapped in heat tape to prevent condensation. The end-cap at the steam outlet was modified from the original design to prevent back flow of oxygen at the 0.5 l/min flow rates by utilizing a high temperature compression fitting to prevent leakage into the alumina tube (Figure 9 a and b). An oxygen sensor was positioned on the outlet line to measure residual oxygen partial pressure (Figure 9a).

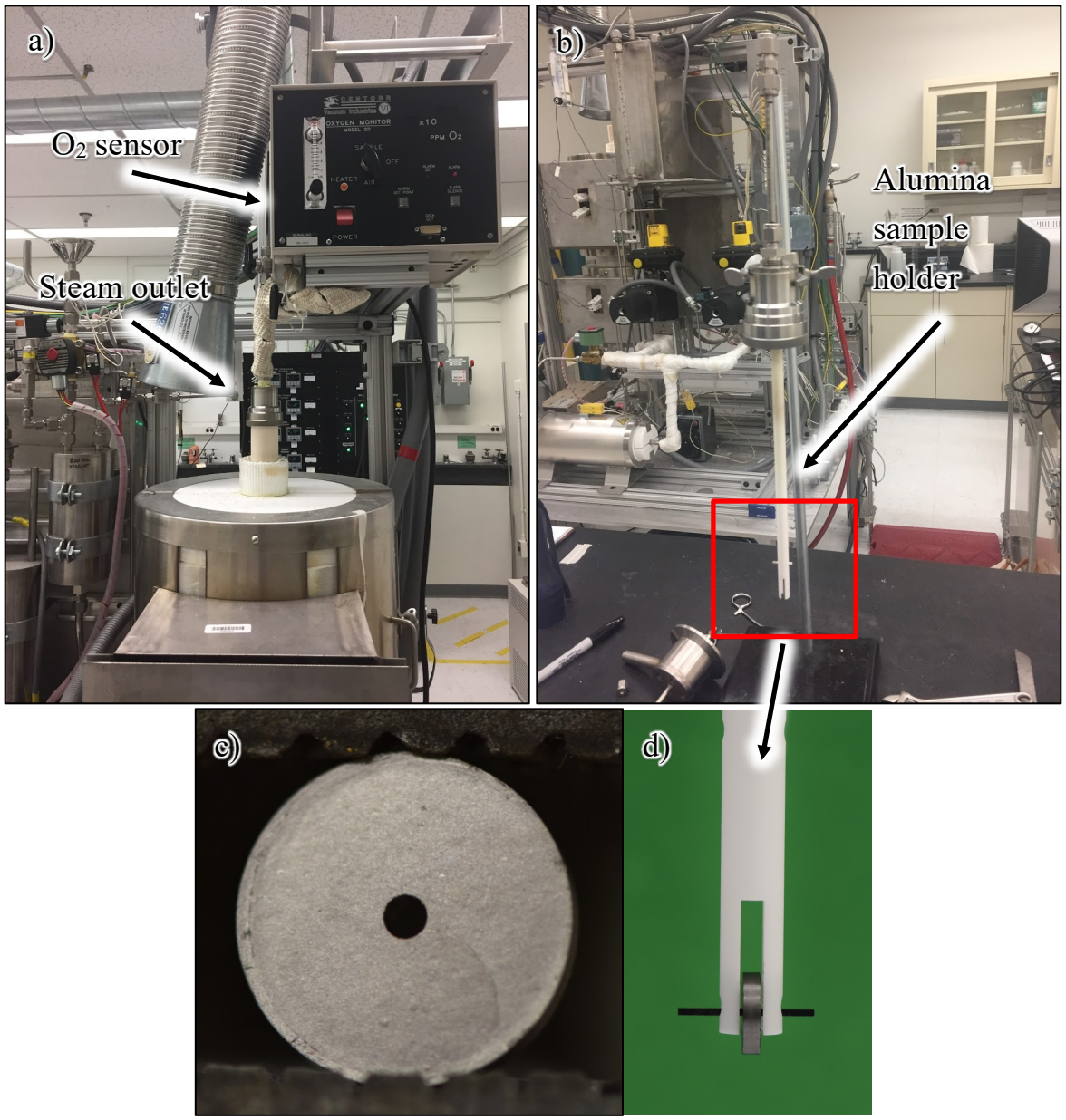

Figure 9. Detailed view of (a) HTM furnace top, (b) alumina sample holder, (c) sample with drilled hole, and (d) sample mounting.

Oxidation behavior was analyzed by directly measuring the change in weight as a function of the exposure condition and time. The matrix-only samples were subjected to a conditioning step per ASTM D7542-09 [25]. This step involved a 130 °C 3 h exposure in air to drive off excess moisture. The samples were then stored in a desiccator and were weighed after conditioning. Weight measurements were made according to AGR program procedures using check weight systems and calibrated balances. The balance was validated before and after each use with a calibrated set of check weights. The aluminum weigh pans used to receive the samples were also measured after oxidation testing, as it was not feasible to handle the samples due to the soft nature of the oxidized material.

The pre-weighed samples were suspended in the furnace system as described above. Prior to starting any run, the system was purged with UHP-He until the residual oxygen's partial pressure (pO_2) was below

300 ppm. Once the furnace reached the appropriate residual oxygen concentrations, the furnace was ramped to temperature at 20 °C/min up to the target temperature. When the appropriate soak temperature was reached, the steam injector was turned on to expose the samples to the water vapor in the UHP-He carrier gas. After the predefined soak time, the steam injector was turned off and the system was cooled to room temperature at a rate of 20 °C/min with UHP-He flowing. After the system had cooled, the oxidized samples were removed from the furnace and dropped into the pre-weighed aluminum weigh pans by sliding the CVD-SiC rod out of the sample. The samples were stored in a desiccator until the weight of the aluminum weigh pans with samples could be measured using the same process as the pre-oxidation measurement. The final weight of the sample was determined by subtracting the weight of the aluminum weigh pan from the total weight. Figure 10 shows a sample before and after oxidation.

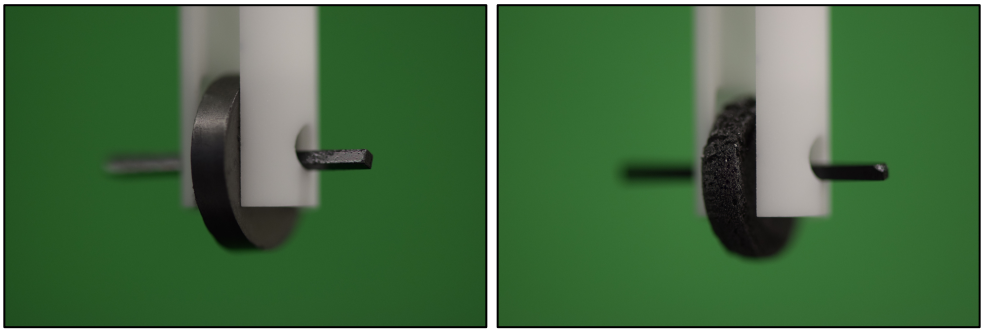

Figure 10. Images of sample before and after oxidation testing showing the change in surface conditions.

The final test matrix is presented in Table 4. An initial maximum temperature of 1,600 °C was sought; however, the oxidation kinetics at these temperatures were too rapid to facilitate testing. Temperatures of 1,200–1,500 °C were analyzed over steam partial pressures (pH_2O) of 10–48 kPa. At least four tests per exposure condition (with a different sample for each test) were performed so that weight change measurements at a minimum of four different exposure times could be obtained. A series of control samples was exposed in UHP-He only at each temperature of interest to establish a baseline oxidation rate associated with the oxidation from residual, contaminant oxygen in the system. Multiple samples were run to determine the oxidation rate from change in weight as a function of time for each condition listed in Table 4. While each sample was assigned a chronological number, samples were randomly assigned for each test. Appendix B lists the change in weight for all oxidation tests, along with other relevant physical measurements (i.e., density and surface area).

Table 4. Test matrix for high temperature steam oxidation tests.

Steam/temperature		1,200 °C	1,300 °C	1,400 °C	1,500 °C
pH_2O (kPa)	0*	✓	✓	✓	✓
	10	✓	✓	✓	✓
	20	✓	✓	✓	
	30	✓	✓	✓	
	48	✓			

*Baseline run to determine contribution from residual oxygen

After oxidation, select samples were subjected to cross sectioning and optical microscopy. The analysis was intended to provide insights into the oxidation behavior of the matrix-only samples at high temperatures. The optical microscopy effort also provides insight into the role of microstructural features on oxidation performance. The samples included in the optical microscopy are listed in Table 5.

Table 5. Samples subjected to cross sectioning and optical microscopy (sample ID, temperature, exposure time, P_{H2O}).

SE-020, 1,200 °C, 1 h, 10 kPa	SE-001, 1,200 °C, 1 h, 20 kPa	SE-113, 1,200 °C, 1 h, 30 kPa
SE-198, 1,200 °C, 1 h, 48 kPa	SE-149, 1,300 °C, 0.25 h, 20 kPa	SE-078, 1,300 °C, 0.5 h, 20 kPa
SE-133, 1,300 °C, 1 h, 20 kPa	SE-098, 1,300 °C, 1.5 h, 20 kPa	SE-064, 1,400 °C, 1 h, 20 kPa
SE-242, as-fabricated		

2.3 DATA ANALYSIS

2.3.1 Data Analysis for Oxidation Kinetics Evaluation

A total of 184 rate values were measured at the various temperatures (800–1,200 °C) and gas compositions (20 Pa < P_{H2O} < 1,000 Pa, 0 < P_{H2} < 100 Pa). Appendix C shows the individual rate values measured at each test conditions. The kinetic parameters were determined following the same process used to determine kinetic parameters for the LH and BLH models from nuclear-grade graphite [13]. The following description of the data analysis approach is mostly reproduced from a technical report by Contescu et al. [13].

To measure the kinetic parameters for LH and BLH models, all valid data were simultaneously analyzed by solving a set of multiple nonlinear rate equations based on the global oxidation reaction, from which the most probable parameter values were found by minimization of the sum of squared errors (SSE) for Y = log (*Rate*), where Y is the rate measured at any given condition, and *Rate* is the weight-normalized oxidation rate ($mg_{oxidized}$ / $mg_{initial}$/ s, or s^{-1}). Two different rate equations were used for data analysis of the LH and BLH models, as follows:

• Classical LH equation [10,19]:

$$\boldsymbol{Rate_{LH}(P_{H2O}P_{H2},T)} = \frac{\boldsymbol{k_1 P_{H2O}}}{\boldsymbol{1+k_2(P_{H2})^{0.5}+k_3 P_{H2O}}} \tag{2}$$

$$\boldsymbol{k_i = A_i exp\left(-\frac{E_i}{RT}\right)} \tag{3}$$

In these equations, T is the temperature (K), E is the activation energy ($J \cdot mol^{-1}$), k_i represents the three rate constants (for i = 1, 2, and 3), and R is the gas constant (8.314 $J \cdot mol^{-1} \cdot K^{-1}$). This kinetic model has six parameters which must be estimated by fitting all data: three preexponential factors (A_i, i = 1,2,3) and three apparent activation energies (E_i, i = 1,2,3).

• The BLH model [16,26]:

$$\boldsymbol{Rate_{BLH}(P_{H2O}P_{H2},T)} = \frac{\boldsymbol{k_1(P_{H2O})^{m(T)}}}{\boldsymbol{1+k_2(P_{H2})^{0.5}+k_3(P_{H2O})^{m(T)}}} \tag{4}$$

$$\boldsymbol{k_i = A_i exp\left(-\frac{E_i}{RT}\right)} \tag{5}$$

$$\boldsymbol{m(T) = m_{max} + \frac{m_{min}-m_{max}}{1+exp\left(\frac{T-T_0}{\theta}\right)}} \tag{6}$$

The BLH kinetic model [16,26] was developed to account for the faster increase of oxidation rates at water vapor pressures >100 Pa and temperatures >950 °C relative to that predicted by the LH model. These differences between the experimental rates and those predicted by the LH model were observed in prior studies on medium grain (PCEA, NBG-17), superfine grain (IG-110) graphite, and superfine grain

(Graphite 2114) graphite in a similar range of oxidant pressures and temperatures [13,26]. The BLH model was introduced to represent all data with a unique, more robust model. The BLH model accounts for this increased rate by introducing a correction to the LH model, assuming that the reaction order for the oxidant (water) depends on temperature, *m(T)*. This dependence, expressed by Equation 6, was best modeled by the integral Boltzmann distribution function with four new parameters: m_{min} and m_{max}, which define the range of apparent reaction order to which a characteristic temperature is associated with the inflection of the *m(T)* function, and θ, which is a scaling parameter equal to the inverse slope of *m(T)* at T_o. With these changes, the BLH model has ten parameters that must be estimated from the collected data.

2.3.2 Data Analysis for High-Temperature/High Partial Pressure Empirical Oxidation

Multiple time intervals were run for each test condition listed in Table 4 with a new sample for each run. The normalized weight loss was calculated from the difference in weight pre- and post-oxidation, divided by the pre-oxidation weight. The contribution to weight loss from residual oxygen in the system was determined by applying a linear fit to the baseline (P_{H20} = 0 kPa) tests for each of the temperatures of interests. This linear relationship was used to determine the normalized weight loss at equivalent exposure conditions for P_{H20} = 10–48 kPa. The weight-normalized contribution to weight loss from the residual oxygen calculated from the linear fit was subtracted from the measured weight loss for the oxidized samples at equivalent exposure conditions to obtain an adjusted weight loss for each condition. Figure 11 illustrates this adjustment for 1200 °C, 10 kPa exposures.

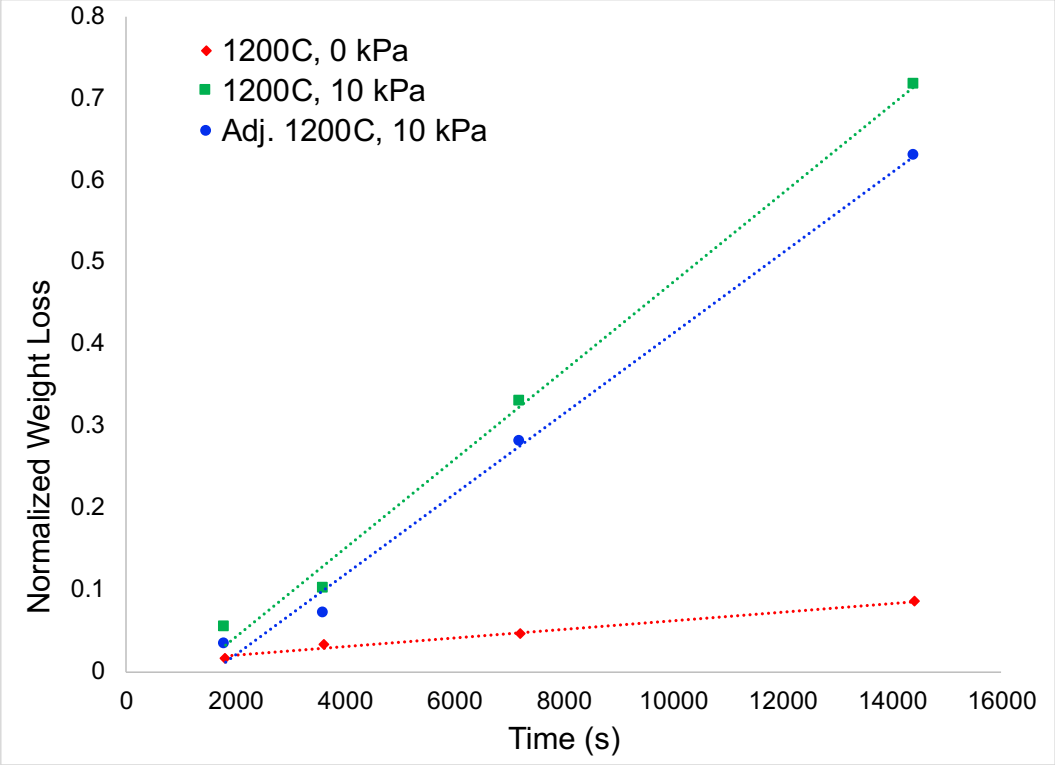

Figure 11. Adjusted weight loss to account for residual oxygen in the system.

The weight normalized oxidation rate (s^{-1}) was determined for each condition by a linear fit of the adjusted weight loss for each condition at a specific temperature and P_{H20}, where the slope of the fit is the rate in reciprocal seconds (s^{-1}). The standard error for the oxidation rate was determined by a least-square fit of data at each measured condition.

3. RESULTS

3.1 RESULTS FOR OXIDATION KINETICS EVALUATION

Appendix C provides the oxidation rate data acquired through testing and the corresponding test conditions. The rate data over the range of analyzed conditions (P_{H2O}, P_{H2}, T) were fit to the analytical solution in Equation 7 and Equation 8 for the LH and BLH models, respectively. Equation 7 and Equation 8 were obtained by combining the equations presented in Section 2.3.1, which describe the LH (Equation 2 and Equation 3) and BLH (Equation 4–Equation 6) models. From this fit, the preexponential factors (A_i) and apparent activation energies (E_i) for each term can be obtained, along with the apparent reactor order ($m(T)$). Figure 12 shows the LH and BLH fit to the experimental oxidation rate data for 16 Pa < P_{H2O} < 688 Pa, P_{H2} = 0, and 850 °C < T < 1,200 °C where the individual data points represent the measured data and the isotherms represent the fits to the analytical solutions.

$$\boldsymbol{Rate_{LH}(P_{H2O}P_{H2},T)} = \frac{\boldsymbol{A_1 exp\left(-\frac{E_1}{RT}\right)(P_{H2O})}}{\boldsymbol{1+A_2 exp\left(-\frac{E_2}{RT}\right)(P_{H2})^{0.5}+A_3 exp\left(-\frac{E_3}{RT}\right)(P_{H2O})}} \tag{7}$$

$$\boldsymbol{Rate_{BLH}(P_{H2O}P_{H2},T)} = \frac{\boldsymbol{A_1 exp\left(-\frac{E_1}{RT}\right)(P_{H2O})^{\left[m_{max}+\frac{m_{min}-m_{max}}{1+exp\left(\frac{T-T_0}{\theta}\right)}\right]}}}{\boldsymbol{1+A_2 exp\left(-\frac{E_2}{RT}\right)(P_{H2})^{0.5}+A_3 exp\left(-\frac{E_3}{RT}\right)(P_{H2O})^{\left[m_{max}+\frac{m_{min}-m_{max}}{1+exp\left(\frac{T-T_0}{\theta}\right)}\right]}}} \tag{8}$$

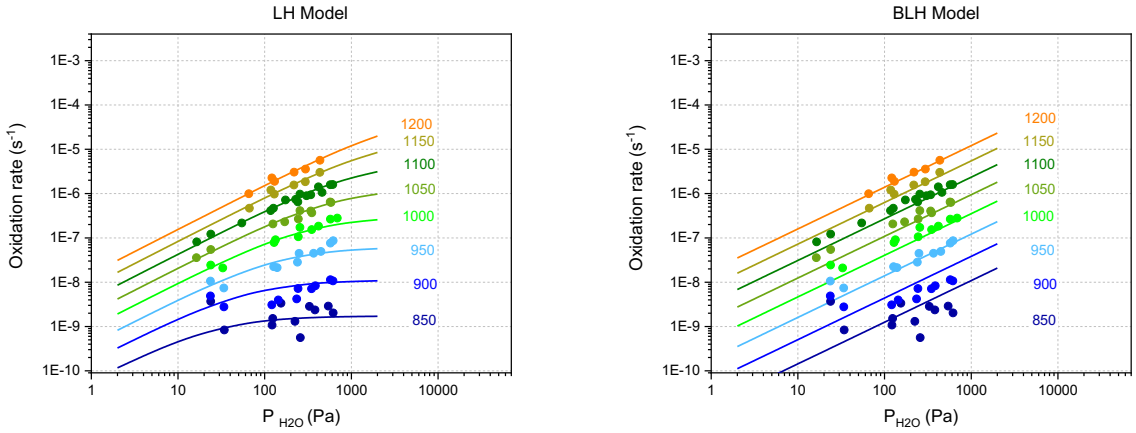

Figure 12. Experimental oxidations rates at P_{H2} = 0 with isothermal trend lines reflecting kinetic parameters determined from best fit for LH (left) and BLH (right) models.

The parameters for both LH and BLH models are listed in Table 6. The parameters were determined by a least squares analysis based on the minimization of the SSE for ln(*Rate*) [13]. Comparison of the isothermal trend lines in Figure 12 suggests that at higher temperature (>950 °C) and at higher pressures (P_{H2O} > 200 Pa), the BLH model better represents the data, while at lower temperatures and pressures, the LH better represents the data. This suggested trend was previously observed for nuclear-grade graphite, but the variation at higher temperatures and pressures was more pronounced than that suggested in this data set [26].

Table 6. Experimentally determined kinetic parameters for LH and BLH models

LH model		BLH model			
A_1	2.8E-2 $(Pa)^{-1}$	A_1	1.1E+2 $(Pa \cdot s)^{-m}$	m_{max}	0.94
A_2	4.0E-10 $(Pa)^{-0.5}$	A_2	6.6E-5 $(Pa)^{-0.5}$	m_{min}	0.11
A_3	2.1E-16 $(Pa)^{-1}$	A_3	3.4E-4 $(Pa)^{-m}$	T_o	1146 K
E_1	181 kJ/mol	E_1	276 kJ/mol	θ	75 K
E_2	-223 kJ/mol	E_2	-87 kJ/mol		
E_3	-318 kJ/mol	E_3	42 kJ/mol		

The quality of fit for the LH and BLH models is shown in Figure 13. The double logarithmic plot compares the observed rate to the predicted rate for the same test conditions for both oxidation tests with H_2 present (red circles) and without H_2 present (blue circles). The quality of fit is represented by the correlation coefficient (R^2) for the linear fit of the data. Perfect agreement follows a linear relationship with $R^2 = 1.0$. The R^2 value for the LH fit was 0.98, and for the BLH fit it was 0.97. This indicates both models represent the data accurately over the range of conditions studied. The suggestion that the BLH model represents the data better at higher temperatures and higher pressures indicates the quality of fit at the higher rates (> 1E-7) compared to the lower rates (< 1E-7). Here, the higher rates are associated with higher temperatures and pressures, where less scatter is observed, as compared to the rates associated with lower temperatures and pressures, where more scatter is observed. There is less scatter in the data at the lower rates (< 1E-7) for the LH model than for the BLH model. This suggests that the LH model is a better representation of low P_{H2O} and low T, while the BLH model is a better representation at high P_{H2O} and high T.

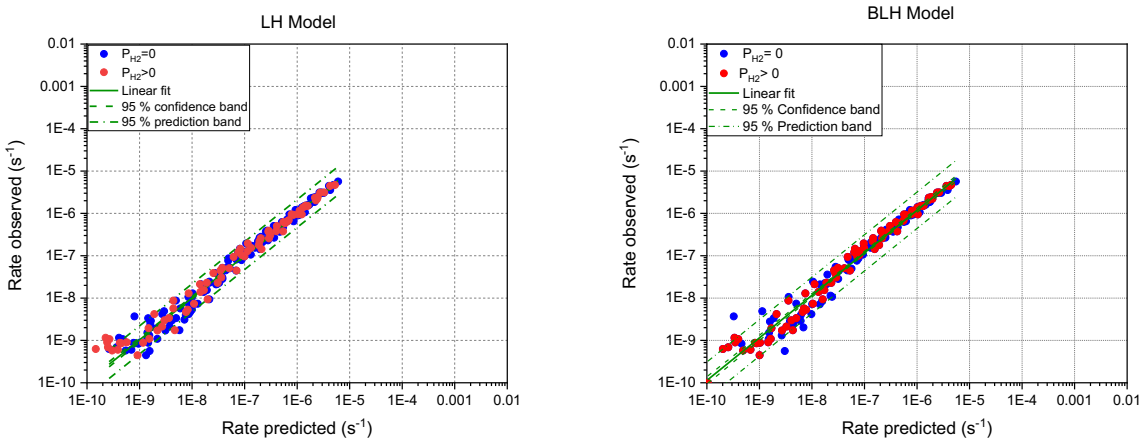

Figure 13. Observed vs. predicted rates for measured oxidation data for the LH and BLH models.

3.2 RESULTS FOR HIGH-TEMPERATURE EMPIRICAL OXIDATION

The normalized weight loss as a function of exposure time shows the impact of temperature and P_{H2O} on oxidation at test conditions relevant to accident conditions. Figure 14 through Figure 16 show normalized weight loss as a function of time for 1,200 °C, 1,300 °C, and 1,400 °C over the range of P_{H2O} analyzed for each temperature. Figure 17 shows the oxidation behavior at P_{H2O} = 10 kPa from 1,200–1,500 °C to illustrate the impact of temperature at a constant P_{H2O}. A linear fit was applied to the data to determine the oxidation rate (s^{-1}), as discussed in Section 2.3.2 (Table 7 lists rate analysis and associated uncertainty of the fit). The analysis indicates that the oxidation rate increases with increasing P_{H2O} up to 30 kPa. Testing at 1,200 °C analyzed P_{H2O} > 30 kPa. The results at 1,200 °C showed that the rate at P_{H2O} = 48 kPa was similar to the rate at P_{H2O} = 30 kPa, suggesting a saturation effect above P_{H2O} = 30 kPa. The constant

pressure analysis shown in Figure 17 highlights the overall impact of temperature. This analysis clearly indicates that oxidation increases with increasing temperature, as expected in a kinetic process. Multiple tests were run for select conditions at P_{H2O} = 20 kPa to determine the repeatability of the analyses. Variation in the measured normalized weight loss was observed. The variability is not expected to be due to density differences. At 1,200 °C, P_{H2O} = 20 kPa, 2 h exposures, the densities of the three samples ranged from 1.783–1.792 g/cm^3, which represents a 0.33–0.84% difference in density. However, this does not reflect the overall increase in weight loss observed across the three samples, which showed a ~49% difference in magnitude between the lowest recorded weight loss and the maximum weight loss for the analyzed condition. The variation is expected to be associated with microstructural feature variation such as exposed pore structure and fissures.

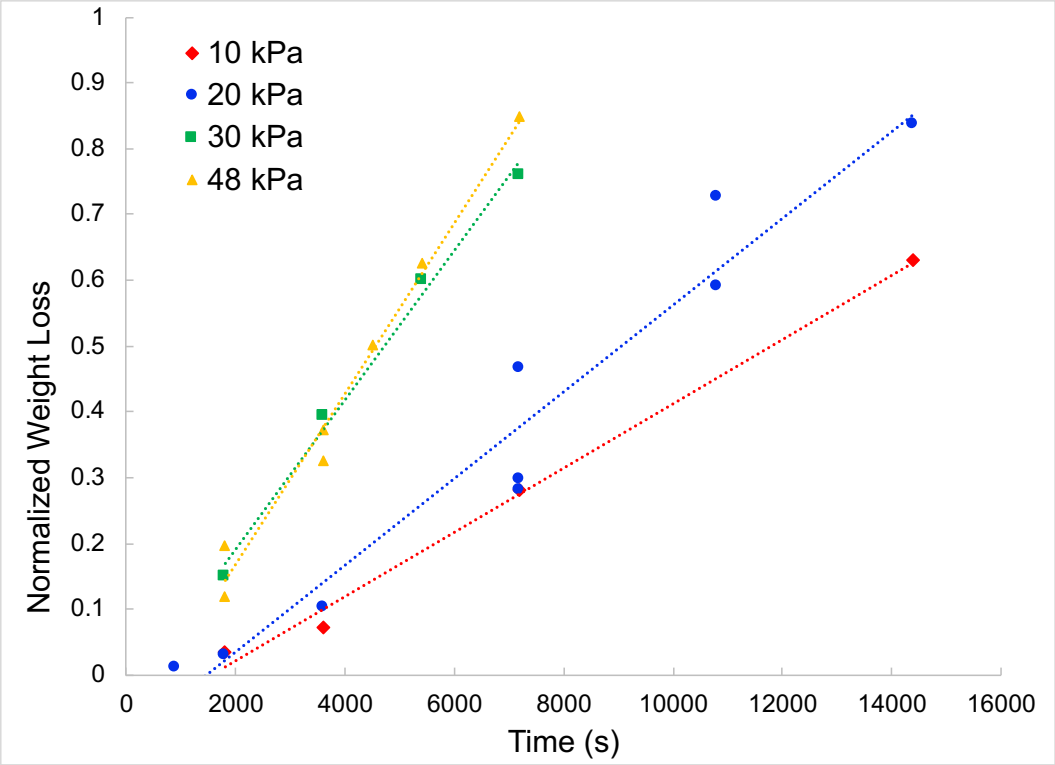

Figure 14. Normalized weight loss as a function P_{H2O} at 1,200 °C.

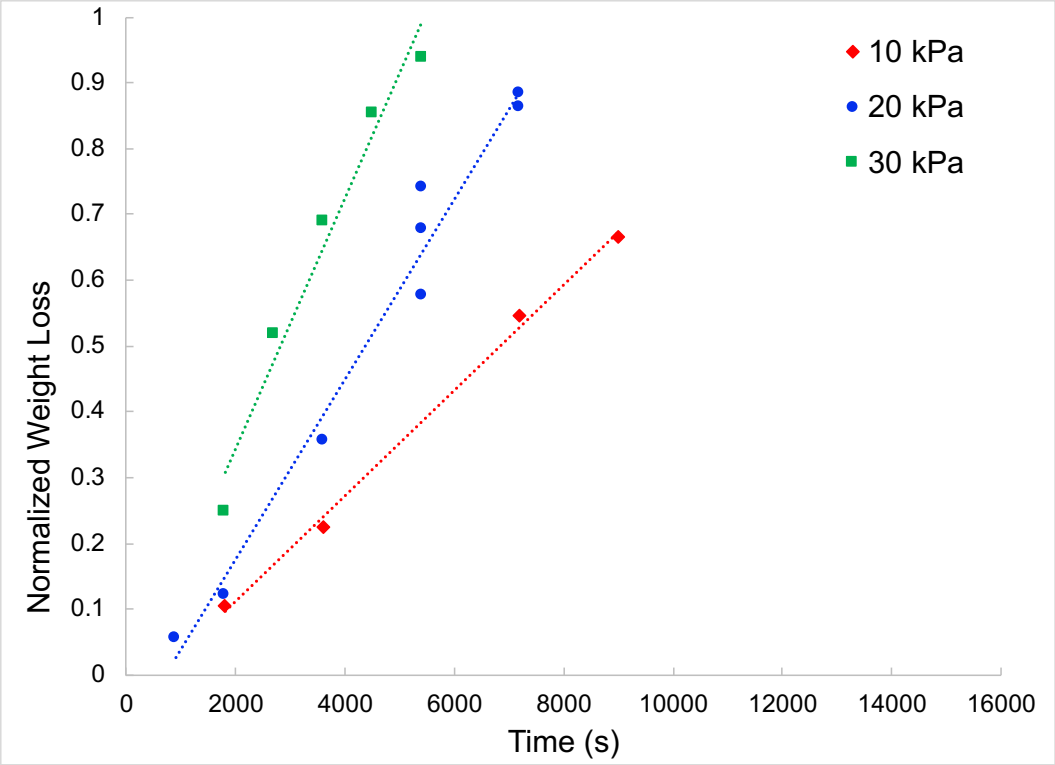

Figure 15. Normalized weight loss as a function P_{H2O} at 1,300 °C

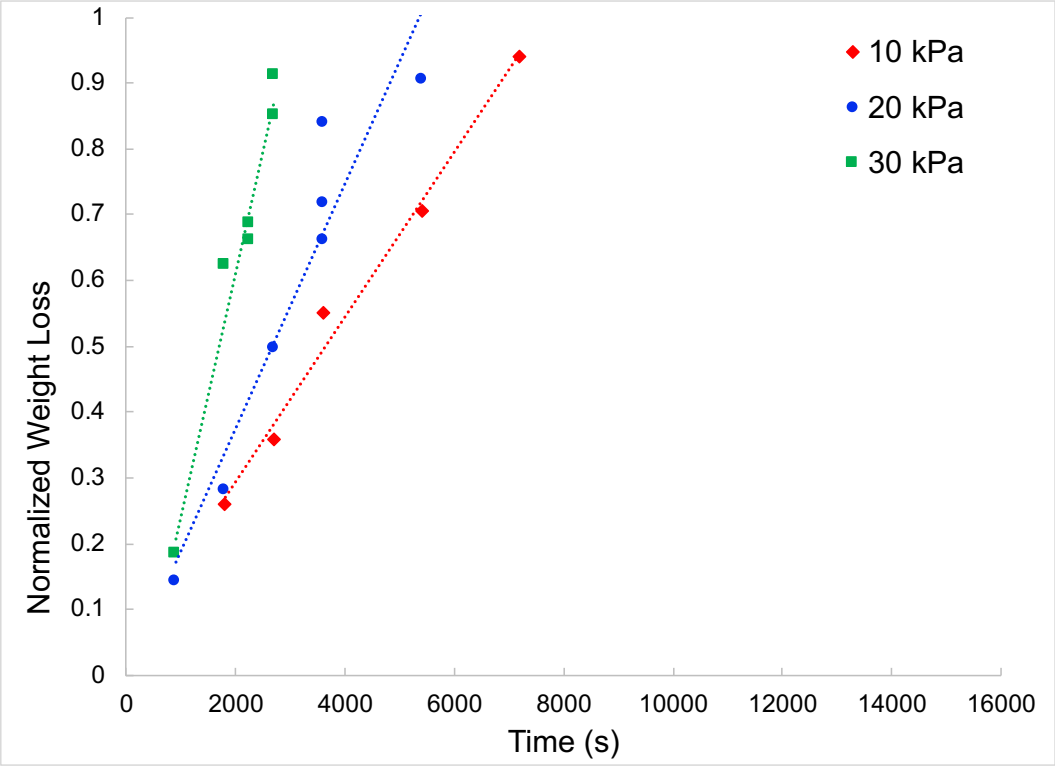

Figure 16. Normalized weight loss as a function P_{H2O} at 1,400 °C

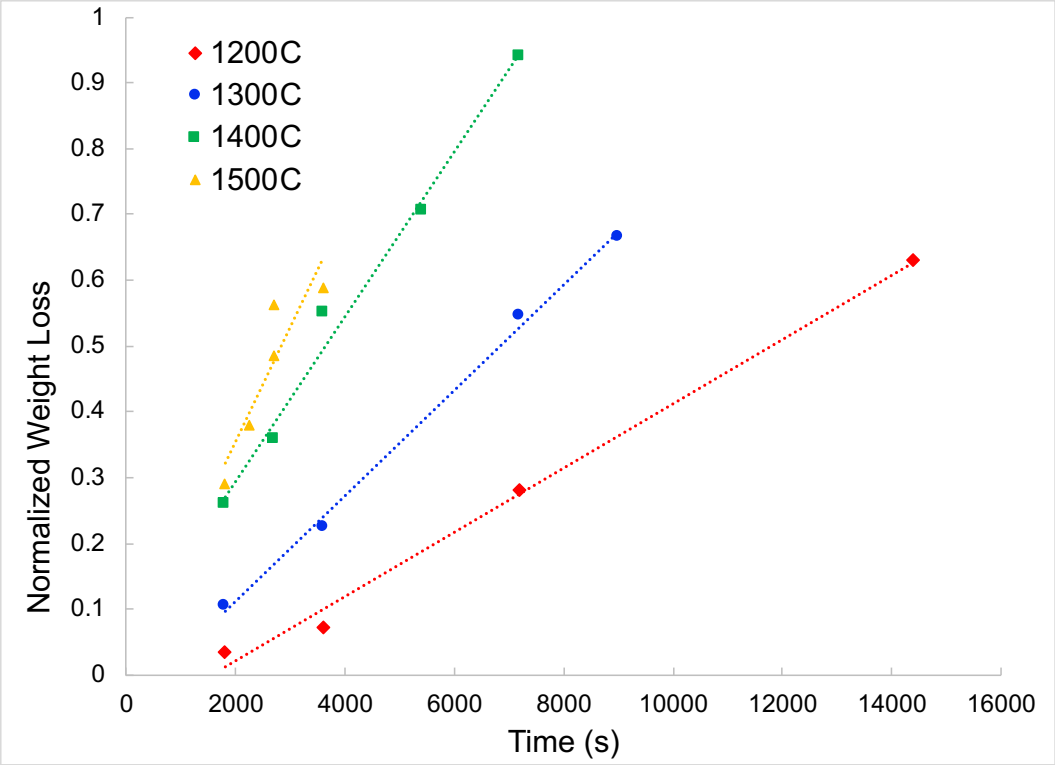

Figure 17. Normalized weight loss as a function temperature (1,200–1,500 °C) at constant P_{H2O} (P_{H2O} = 10 kPa).

The measured rates are presented in Table 7 and illustrated in Figure 18. The measured rates were fit to an Arrhenius relationship defining an effective rate equation for each P_{H2O} analyzed, equivalent to (3. Table 8 lists the activation energy (E) and pre-exponential term (A) associated with the Arrhenius relationship. The Arrhenius relationship is empirically derived and appropriate only over the range of conditions (including oxidant flow rate) analyzed.

Table 7. Rate analysis for high-temperature oxidation testing.

Temperature (°C)	P_{H2O} (kPa)	Rate (s^{-1})*	$R^{2\wedge}$
1200	10	$4.89\pm0.26\times10^{-5}$	0.99
1200	20	$6.59\pm0.60\times10^{-5}$	0.95
1200	30	$1.13\pm0.07\times10^{-4}$	0.99
1200	48	$1.30\pm0.08\times10^{-4}$	0.98
1300	10	$8.03\pm0.32\times10^{-5}$	1.00
1300	20	$1.37\pm0.09\times10^{-4}$	0.97
1300	30	$1.90\pm0.21\times10^{-4}$	0.97
1400	10	$1.25\pm0.09\times10^{-4}$	0.99
1400	20	$1.86\pm0.26\times10^{-4}$	0.91
1400	30	$3.71\pm0.36\times10^{-4}$	0.96
1500	10	$1.71\pm0.45\times10^{-4}$	0.83

*error reported in standard error from linear regression analysis
^R^2 value is rounded to two significant figures

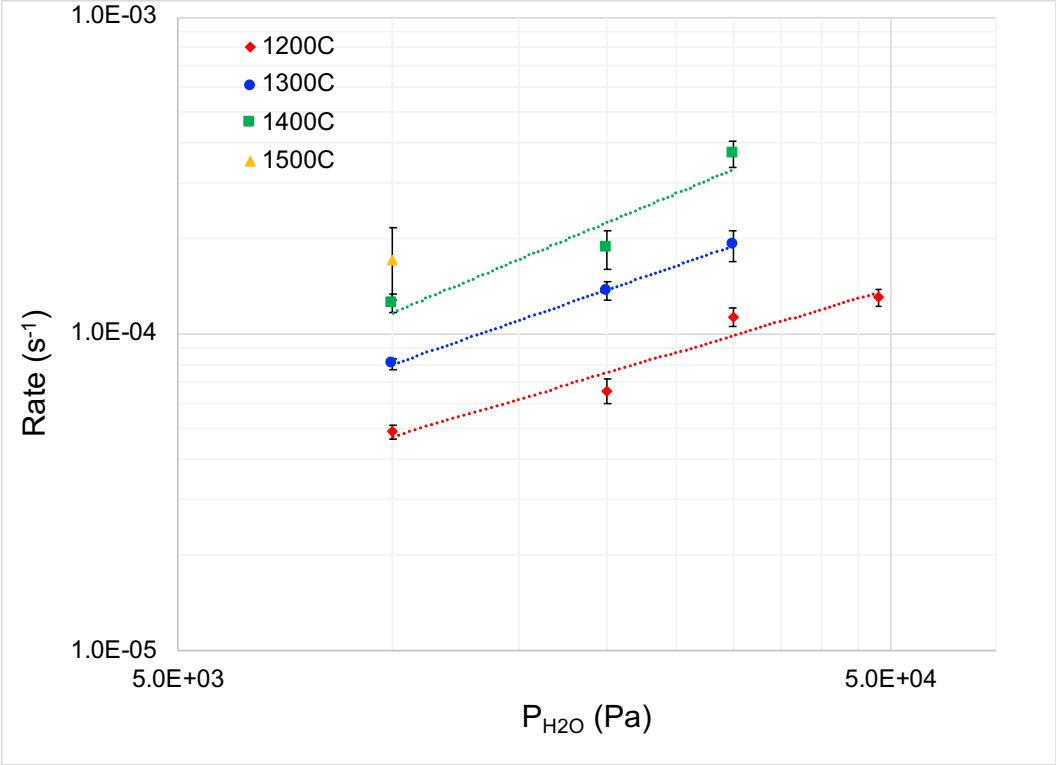

Figure 18. Measured oxidation rate as a function of P_{H2O}.

Table 8. Effective oxidation kinetics for matrix-only samples in high-temperature steam.

P_{H2O} (kPa)	A (s^{-1})	E (kJ/mol)
10	0.09	91.6
20	0.43	107.1
30	2.18	121.3

Select samples were axially cross sectioned and optically imaged to show the nature of the oxidation behavior. Figure 19 shows a series of optical micrographs from an as-fabricated sample and from samples exposed to 1,200 °C for 1 h at different P_{H2O} (20–48 kPa). Appendix D shows optical micrographs from all that were samples subjected to cross sectional analysis. Fissures running perpendicular to the pressing direction were identified in the as-fabricated samples (Figure 19a). The presence of fissures was not unexpected based on previous observations for this matrix recipe [23]. A uniform oxidation layer is apparent around the outer surface of the oxidized samples (Figure 19b–d) with an apparently unaffected central region. Localized oxidation penetrating the bulk was also observed along the inner surface of fissures interesting the surface. This oxidized region appears to have a lower overall density relative to the bulk. The low-density oxidized regions are indicated by a darker color (relative to the bulk) and increased porosity, while pores that are not back-filled with epoxy appear black. The fissures serve as pathways for oxidation to penetrate the interior of the sample. Clear evidence of this is shown in the close-up micrograph in Figure 20a, in which oxidation has preferentially occurred along the exposed surface of the fissure which has intersected the sample surface. The samples exposed to higher P_{H2O} show significant oxidation along the fissures, leading to nonuniform oxidation of the sample. Close-up micrographs of the oxidation regions are shown in Figure 20b; the low-density oxidized material shows flake-like grains surrounded by epoxy, with an apparent gradient from loose graphitic flake to dense matrix material moving from exposed surfaces toward the bulk which has not experienced significant oxidation.

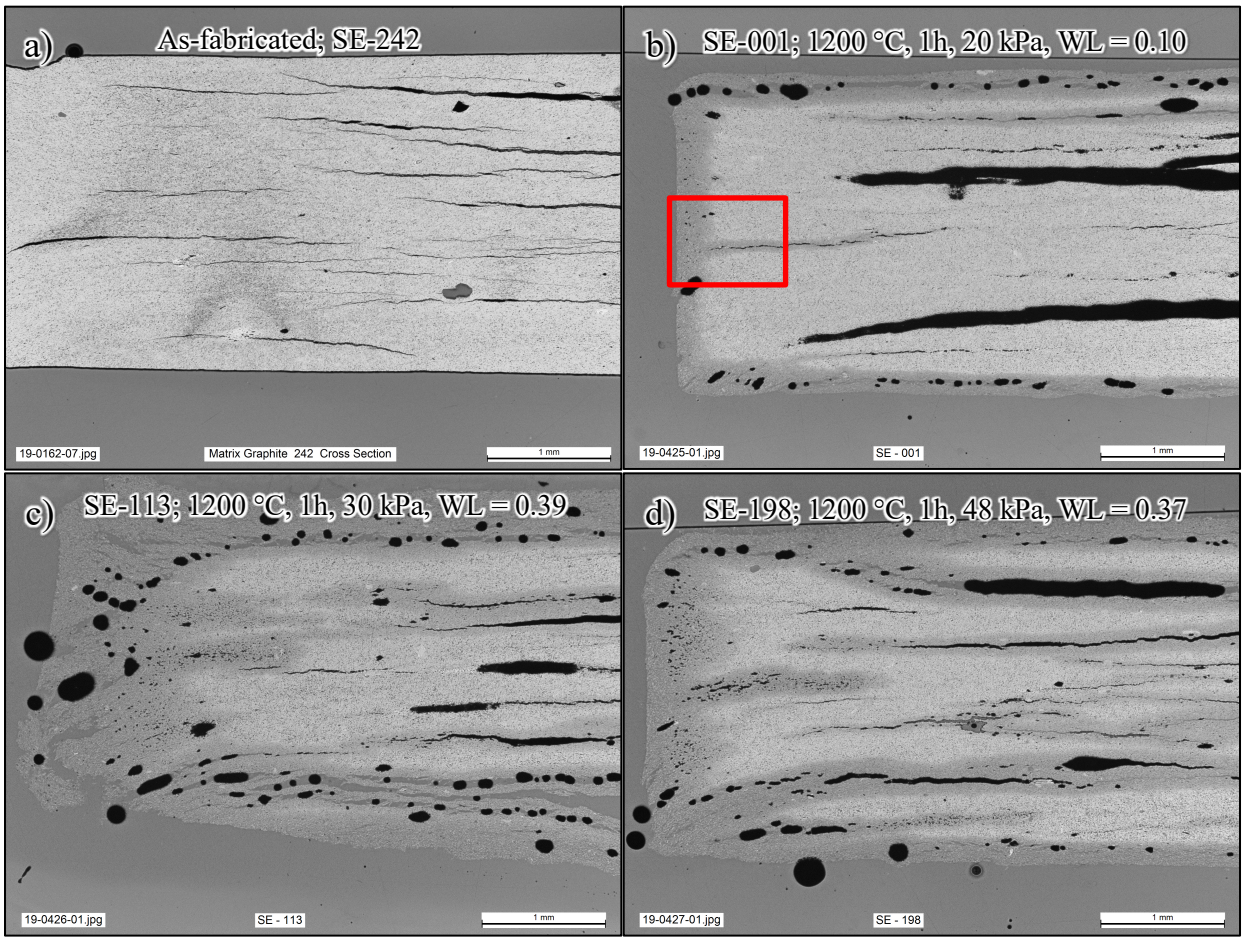

Figure 19. Overview micrographs of the cross section of the an-fabricated and select oxidized samples at 1,200 °C, 1 h, and varying P_{H2O}, showing the impact of macroscopic fissures on oxidation behavior in the high-temperature oxidation testing (red box identifies the approximate area of interest presented in Figure 20; black regions are pores not filled by epoxy; *WL* is measured, normalized weight loss.

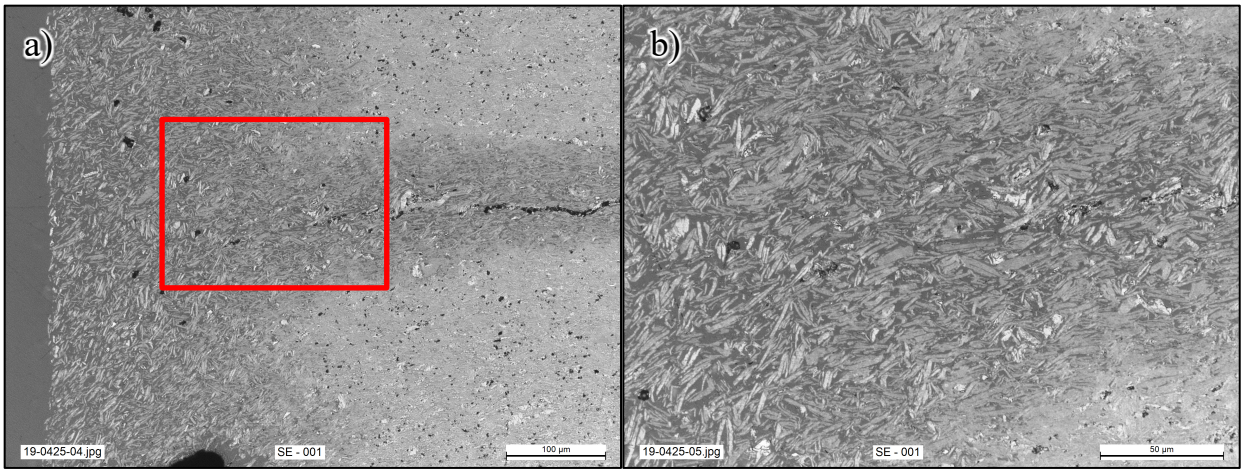

Figure 20. Close-up micrographs highlighting (a) penetration along the exposed fissures and (b) low-density oxidized region showing apparent residual graphite flake; the red box highlights the approximate area of interest shown in (b) in the higher magnification micrograph from SE-001 (1,200 °C, 1 h, P_{H2O} = 20 kPa).

The preferential oxidation observed at the surface confirms that the oxidation reaction is beyond the purely kinetic regime. Based on the optical micrographs, the system appears to be in the transition regime (Figure 1), as there is clearly a partially oxidized region penetrating from the surface. However, the matrix-only samples are not a heterogenous material, consisting of a partially graphitized resin binder, natural graphite flake, and synthetic graphite flake. Each of these components is expected to have a different oxidation response. Because of the composite nature of the matrix-only samples, it is possible that the reaction is in the diffusion-controlled regime for the partially graphitized resin binder and in the transition regime for the graphite flake components, as they appear to preferentially remain in the low-density, oxidized regions.

The optical micrographs confirm the influence of exposed surface area on the oxidation behavior. The distribution of fissures in the samples likely explains the observed sample variance in high-temperature empirical oxidation tests. Here the presence of exposed fissures increases the effective surface area. In the kinetic regime, this would not impact the results, as the oxidation occurs uniformly. However, in the transition and diffusion-controlled regimes, the oxidation reaction is surface dependent, so the increased effective surface area will lead to an increase in the effective oxidation rate for the sample.

The high-temperature empirical oxidation rate data for 1,200–1,400 °C obtained from tests in the HTM were compared with the oxidation kinetics data from the lower-temperature TAG analysis in Figure 21. Figure 21 shows the LH and BLH models fit to the data acquired from the TAG analysis, which produced the kinetic parameters listed in Table 6. The data points below 1,000 Pa are from the TAG analysis, and the LH and BLH models were fit to these data. The data points for $P_{H2O} \geq 10{,}000$ Pa from the HTM tests were plotted and compared to the LH and BLH model predictions. Figure 22 shows the observed vs. predicted rates for measured oxidation data for the LH and BLH models, with high-temperature empirical oxidation results included. The correlation coefficient (R^2) for each fit with the high temperature data included is 0.98 for the LH model and 0.97 for the BLH model. The BLH model shows good agreement with the 1,200 °C data based on the comparison of the predicted rate vs. the measured oxidation rate. This would corroborate the assessment that the BLH model better captures the oxidation behavior at higher temperatures and P_{H2O} [13]. The appropriateness of the BLH model at 1,200 °C should be questioned, as the destructive analysis indicates that the samples are beyond the kinetic regime. This is supported for the higher temperature conditions in which both models overpredict the oxidation rates at 1,300 °C and 1,400 °C. This is expected to be a result of the oxidation no longer being in the kinetic regime at the elevated temperatures. The optical micrographs indicate that oxidation was in the transition regime where both chemical kinetic and mass transfer phenomena are significant. An accurate model for that regime would have to include both of these effects.

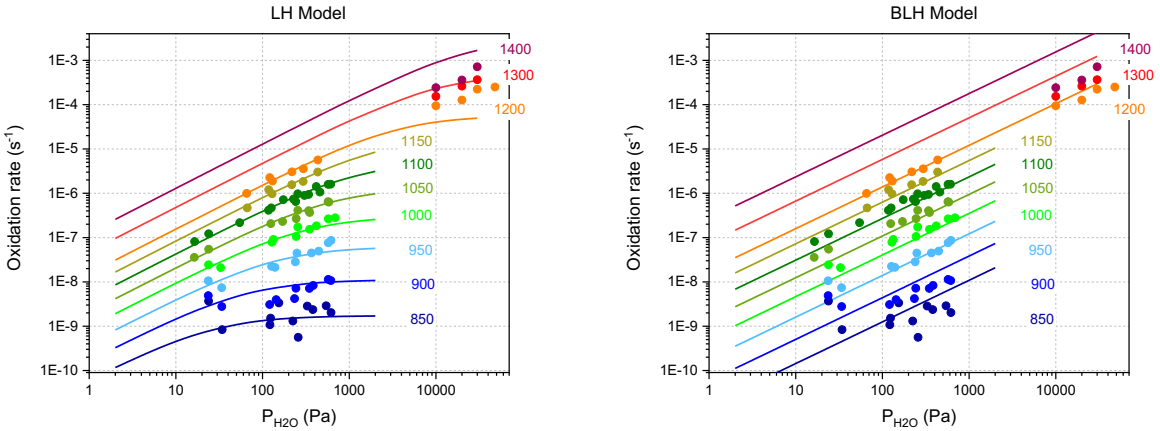

Figure 21. Experimental oxidations rates at P_{H2} = 0 with isothermal trend lines reflecting kinetic parameters determined from best fit for LH (left) and BLH (right) models with high-temperature empirical oxidation results included.

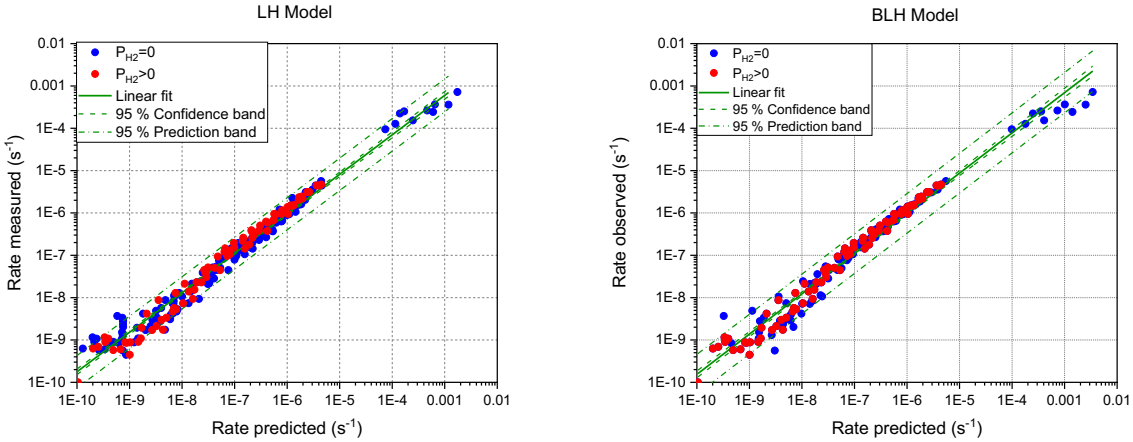

Figure 22. Observed versus predicted rate for measured oxidation data for the LH and BLH models with high-temperature empirical oxidation results included.

4. SUMMARY

This study established separate-effects testing of the oxidation performance of HTGR matrix material in varied moisture environments. Matrix-only samples were produced specifically for this investigation, with properties near representative of the AGR-5/6/7 pedigree and with density serving as the primary target and minimal fissuring as the secondary target. Investigation of the oxidation behavior was conducted over a wide range of oxidation conditions that spanned the kinetic regime and beyond. The range in conditions allowed for analysis of the chemical oxidation kinetics and the conditions relevant to extreme accident scenarios. The oxidation rate data in the oxidation kinetics evaluation were fit to two established models—LH and BLH—to determine the kinetic parameters (Table 6). Both models fit the data reasonably well, with the LH model better representing the data at low temperatures and pressures (P_{H2O}), and the BLH model better representing the data at higher temperatures and pressures (P_{H2O}). This observation is consistent with prior analysis conducted for nuclear grade graphite. Ultimately, the obtained kinetic parameters can be leveraged in fuel performance models to determine the response of

matrix material in various scenarios involving moisture ingress. The empirical oxidation testing at high temperatures ($1200 \leq T \leq 1500°C$) and high pressures ($P_{H2O} \geq 10$ kPa) showed the expected trends, with increasing oxidation rate as a function of temperature. At a constant temperature, the testing showed oxidation rates increased with increasing P_{H2O}, with apparent saturation beginning at ~30 kPa. An Arrhenius relationship was fit to the varying oxidation rates according variable P_{H2O} at a given temperature. Comparison of the empirical high-temperature/high-P_{H2O} oxidation rates with the LH and BLH models showed that the models overpredicted the oxidation rate. This is justified, since a departure from the kinetic regimes into a diffusion dependent regime (*transition or diffusion-controlled regime*) is expected and was confirmed based on the observed deviation from the LH and BLH fits and by the surface dependence of the oxidation reaction shown in the optical microscopy of cross sectioned samples. This destructive analysis also highlighted the composite nature of the matrix-only samples, in which apparent selective oxidation of the carbonized resin binder is occurring, as residual graphite flake material appears to be remaining in the oxidized surface regions. Furthermore, the fissures in the samples acted as pathways for transport of oxidants from the sample surface to its interior. Differences in the number and structure of fissures from sample-to-sample also led to apparent variation in sample oxidation rate at high-temperatures/partial pressures beyond the kinetic regime. Sample-to-sample variation was not observed in the kinetic regime tests because kinetic oxidation occurs more uniformly throughout the sample an is not limited by oxidant mass transport effects that become more significant at higher temperatures.

Future work should target oxidation testing of matrix-only samples without fissures to isolate the high temperature matrix oxidation behavior given the variation of oxidation response in matrix material with fissures during testing beyond the kinetic regime. This testing would be more representative of a separate effects test. Matrix material from AGR-1 and AGR-2 experiments may satisfy this case. A systematic pursuit of matrix formulations, precursor materials (natural and synthetic graphite flake and resin), and processing routes may also be warranted. This would allow the exploration of fully dense material with minimal defects such as fissures or pores as well as materials with different microstructures. The motivation is to understand how the defect structure and matrix microstructure impacts the response to interactions with oxidants. Other areas of relevant pursuit may involve oxidation tests of surrogate fuel compacts containing non-fueled particles to better simulate the exact nature of the fissures in graphitic matrix material of fuel elements.

5. REFERENCES

1. Preliminary Safety Information Document for the Standard MHTGR, Vol. 1, HTGR-86-024, Stone and Webster Engineering Corp., Boston, MA (1986).
2. F.C. Montgomery, "Evaluation of Need for Integral Fuel Oxidation Tests," DOE-HTGR-86-002, GA Technologies, Inc. (1987).
3. Z. Yanhua, S. Lei, and W. Yan, "Water-ingress analysis for the 200 MWe pebble-bed modular high temperature gas-cooled reactor," *Nuclear Engineering and Design*, **240** (2010) 3095–3107.
4. M. Richards, "REACT_COMPACT: A Computer code for Modeling Graphite Corrosion and Fuel Hydrolysis," *Proceedings of the HTR 2016*, Las Vegas, NV, November, (2016).
5. N. Iniotakis, and C.B. von der Decken, "Radiological consequences of a depressurized accident combined with water ingress in an HTR Module-200," *Nuclear Engineering and Design*, **109** (1988) 299–305.
6. G.H. Lohnert, "The consequences of water ingress into the primary circuit of an HTR-Module—From design basis accident to hypothetical postulates," *Nuclear Engineering and Design*, **134** (1992) 159–176.
7. J. Wolters, R. Bongartz, W. Jahn, and R. Moormann, "The Significance of Water Ingress Accidents in Small HTRs," *Nuclear Engineering and Design*, **109**, (1988) 289–294.
8. C. I. Contescu et al., "Practical Aspects for Characterizing Air Oxidation of Graphite," *Journal of Nuclear Materials* **381**, (2008)15–24.
9. J. J. Lee, T. K. Ghosh, and S. K. Loyalka, "Oxidation Rate of Graphitic Matrix Material in the Kinetic Regime for VHTR Air Ingress Accident Scenarios," *Journal of Nuclear Materials* **451** (2014) 48–54.
10. C. Velasquez, G. Hightower, and R. Burnette, "The Oxidation of H-451 Graphite by Steam," GA-A14951, General Atomic Company (1978).
11. L. G. Overholser and J. P. Blakely, "Oxidation of Graphite by Low Concentrations of Water Vapor and Carbon Dioxide in Helium." *Carbon* **2** (1965) 385–394.
12. C. I. Contescu, R. W. Mee, et al., "Oxidation of PCEA Nuclear Graphite by Low Water Concentrations in Helium," *Journal of Nuclear Materials* **453** (2014) 225–232.
13. C. I. Contescu, Y. (Jo Jo) Lee, and R. W. Mee, "Oxidation Kinetics by Water Vapor of Nuclear Grade Graphite Grade 2114," ORNL/TM-2018/1057, Oak Ridge National Laboratory, Oak Ridge, TN (2018).
14. R. C. Giberson and J. P. Walker, "Reaction of Nuclear Graphite with Water Vapor. Part I. Effect of Hydrogen and Water Vapor Partial Pressures, *Carbon* **3** (1966) 521–525.
15. J. J. Kane, C. I. Contescu. R. E. Smith, G. Strydom, and W. E. Windes , "Understanding the Reaction of Nuclear Graphite with Molecular Oxygen: Kinetics, Transport, and Structural Evolution" *Journal of Nuclear Materials* **493** (2017) 343–367.
16. C. I. Contescu and R. Mee, "Status of Chronic Oxidation Studies of Graphite," ORNL/TM-2016/195. Oak Ridge National Laboratory, Oak Ridge, TN (2018).
17. C. I. Contescu, T. D. Burchell, and R. W. Mee, "Accelerated Oxidation Studies of PCEA Nuclear Graphite by Low Concentrations of Water and Hydrogen in Helium," ORNL/TM-2013/524, Oak Ridge National Laboratory, Oak Ridge, TN (2013).
18. C. I. Contescu, T. D. Burchell, and R. W. Mee, "Kinetics of Chronic Oxidation of NBG-17 Nuclear Graphite by Water Vapor," ORNL/TM-2015/142, Oak Ridge National Laboratory, Oak Ridge, TN (2015).
19. P. L. Walker, Jr., F. Rusinko, Jr., and L. G. Austin, "Gas Reactions of Carbon," *Adv. Catalysis* **11** (1959) 133–221.
20. T. H. Hurt and J. M. Calo, "Semi-Global Intrinsic Kinetics for Char Combustion Modeling," *Combustion and Flame* **125** (2001)138–1149.

21. D. W. Marshall, “AGR-5/6/7 Fuel Specification.” SPC-1352-R5, Idaho National Laboratory, Idaho Falls, ID (2015).
22. B. P. Collin, “AGR-5/6/7 Irradiation Experiment Test Plan,” PLN-5245, Idaho National Laboratory, Idaho Falls, ID (2017).
23. M. P. Trammel and B. C. Jolly, “AGC-4 Compact Fabrication Study.” Oak Ridge National Laboratory, Oak Ridge, TN (2014).
24. K. A. Terrani and C. M. Silva, “High Temperature Steam Oxidation of SiC Coating Layer of TRISO Fuel Particles,” *Journal of Nuclear Materials* **460** (2015) 160–165.
25. “Standard Test Method for Air Oxidation of Carbon and Graphite in the Kinetic Regime.” ASTM D7542-09 (2016).
26. C. I. Contescu, R. W. Mee, Y. (Jo Jo) Lee, J. D. Arregui-Mena, N. C. Gallego, T. D. Burchell, J. J. Kane, and W. E. Windes, Beyond the Classical Kinetic Model for Chronic Graphite Oxidation by Moisture in High Temperature Gas-Cooled Reactors,” *Carbon* **127** (2018) 158–169.

APPENDIX A. AS-FABRICATED MATRIX SAMPLE PROPERTIES

Table A-1. As-fabricated matrix-only sample properties and acceptance status. Measured properties include diameter (dia.), density (ρ)^, weight^, and surface area-to-volume ratio (SA:V). All measured properties (except SA:V) represent the mean where σ is the standard deviation.

Sample ID	Dia. (mm)	σ-Dia. (mm)	Length (mm)	σ-Length (mm)	Weight (g)	ρ (g/cm³)	σ-ρ (g/cm³)	SA:V	Status (visual)	Status (ρ)	Status (final)
SE-001	12.156	0.003	2.538	0.012	0.528	1.792	0.001	1:1.12	Accept	Accept	Accept
SE-002	12.147	0.000	2.525	0.006	0.527	1.803	0.006	1:1.12	Accept	Accept	Accept
SE-003	12.151	0.000	2.521	0.003	0.528	1.808	0.003	1:1.12	Reject	Accept	Reject
SE-004	12.143	0.001	2.514	0.016	0.528	1.815	0.016	1:1.13	Reject	Reject	Reject
SE-005	12.143	0.004	2.539	0.012	0.528	1.797	0.012	1:1.12	Reject	Accept	Reject
SE-006	12.132	0.002	2.552	0.007	0.527	1.788	0.007	1:1.11	Reject	Accept	Reject
SE-007	12.153	0.001	2.548	0.013	0.528	1.786	0.013	1:1.11	Accept	Accept	Accept
SE-008	12.157	0.002	2.561	0.007	0.529	1.779	0.007	1:1.11	Reject	Accept	Reject
SE-009	12.146	0.003	2.542	0.009	0.529	1.795	0.009	1:1.12	Reject	Accept	Reject
SE-010	12.152	0.002	2.540	0.005	0.528	1.794	0.005	1:1.12	Accept	Accept	Accept
SE-011	12.146	0.001	2.559	0.000	0.527	1.777	0.000	1:1.11	Reject	Accept	Reject
SE-012	12.135	0.000	2.520	0.014	0.527	1.807	0.014	1:1.12	Accept	Accept	Accept
SE-013	12.148	0.002	2.628	0.009	0.528	1.732	0.009	1:1.09	Reject	Accept	Reject
SE-014	12.138	0.000	2.572	0.016	0.528	1.773	0.016	1:1.11	Reject	Accept	Reject
SE-015	12.137	0.002	2.569	0.004	0.528	1.776	0.004	1:1.11	Reject	Accept	Reject
SE-016	12.119	0.000	2.547	0.011	0.527	1.794	0.011	1:1.12	Reject	Accept	Reject
SE-017	12.152	0.001	2.546	0.012	0.527	1.783	0.012	1:1.11	Reject	Accept	Reject
SE-018	12.145	0.001	2.543	0.002	0.528	1.792	0.002	1:1.12	Accept	Accept	Accept
SE-019	12.149	0.002	2.584	0.006	0.527	1.761	0.006	1:1.10	Reject	Accept	Reject
SE-020	12.151	0.002	2.555	0.012	0.527	1.780	0.012	1:1.11	Accept	Accept	Accept
SE-021	12.152	0.001	2.583	0.011	0.527	1.760	0.011	1:1.10	Reject	Accept	Reject
SE-022	12.166	0.001	2.553	0.010	0.526	1.771	0.010	1:1.11	Reject	Accept	Reject
SE-023	12.171	0.001	2.576	0.023	0.528	1.762	0.023	1:1.11	Accept	Accept	Accept
SE-024	12.151	0.002	2.607	0.015	0.526	1.739	0.015	1:1.10	Reject	Accept	Reject
SE-025	12.158	0.001	2.654	0.014	0.528	1.712	0.014	1:1.08	Reject	Accept	Reject
SE-026	12.155	0.001	2.577	0.007	0.526	1.759	0.007	1:1.11	Accept	Accept	Accept
SE-027	12.154	0.002	2.550	0.004	0.527	1.782	0.004	1:1.11	Reject	Accept	Reject
SE-028	12.140	0.003	2.573	0.010	0.527	1.771	0.010	1:1.11	Reject	Accept	Reject
SE-029	12.145	0.003	2.613	0.004	0.527	1.742	0.004	1:1.09	Accept	Accept	Accept
SE-030	12.160	0.001	2.535	0.003	0.527	1.790	0.003	1:1.12	Accept	Accept	Accept
SE-031	12.149	0.001	2.574	0.002	0.528	1.770	0.002	1:1.11	Reject	Accept	Reject
SE-032	12.132	0.002	2.518	0.005	0.527	1.809	0.005	1:1.12	Accept	Accept	Accept
SE-033	12.170	0.001	2.642	0.015	0.539	1.753	0.015	1:1.09	Reject	Accept	Reject
SE-034	12.176	0.000	2.641	0.002	0.538	1.751	0.002	1:1.09	Reject	Accept	Reject
SE-035	12.147	0.001	2.552	0.014	0.527	1.783	0.014	1:1.11	Accept	Accept	Accept
SE-036	12.189	0.001	2.677	0.001	0.525	1.682	0.001	1:1.08	Accept	Reject	Reject
SE-037	12.164	0.003	2.604	0.013	0.528	1.745	0.013	1:1.10	Reject	Accept	Reject
SE-038	12.164	0.004	2.555	0.011	0.528	1.779	0.011	1:1.11	Accept	Accept	Accept

Sample ID	Dia. (mm)	σ-Dia. (mm)	Length (mm)	σ-Length (mm)	Weight (g)	ρ (g/cm³)	σ-ρ (g/cm³)	SA:V	Status (visual)	Status (ρ)	Status (final)
SE-039	12.138	0.002	2.611	0.008	0.528	1.747	0.008	1:1.10	Accept	Accept	Accept
SE-040	12.152	0.007	2.568	0.015	0.527	1.768	0.015	1:1.11	Accept	Accept	Accept
SE-041	12.479	0.233	2.596	0.006	0.526	1.655	0.006	1:1.09	Reject	Reject	Reject
SE-042	12.193	0.002	2.760	0.016	0.522	1.620	0.016	1:1.05	Reject	Reject	Reject
SE-043	12.132	0.002	2.588	0.010	0.528	1.765	0.010	1:1.10	Reject	Accept	Reject
SE-044	12.138	0.002	2.544	0.016	0.528	1.792	0.016	1:1.12	Reject	Accept	Reject
SE-045	12.137	0.000	2.561	0.011	0.527	1.780	0.011	1:1.11	Reject	Accept	Reject
SE-046	12.146	0.001	2.515	0.004	0.527	1.808	0.004	1:1.12	Reject	Accept	Reject
SE-047	12.135	0.003	2.531	0.010	0.528	1.803	0.010	1:1.12	Reject	Accept	Reject
SE-048	12.131	0.004	2.522	0.009	0.527	1.808	0.009	1:1.12	Reject	Accept	Reject
SE-049	12.128	0.003	2.619	0.022	0.527	1.743	0.022	1:1.09	Reject	Accept	Reject
SE-050	12.127	0.000	2.580	0.010	0.527	1.770	0.010	1:1.11	Reject	Accept	Reject
SE-051	12.134	0.004	2.567	0.003	0.529	1.781	0.003	1:1.11	Reject	Accept	Reject
SE-052	12.142	0.003	2.535	0.005	0.528	1.799	0.005	1:1.12	Accept	Accept	Accept
SE-053	12.121	0.005	2.541	0.013	0.529	1.802	0.013	1:1.12	Accept	Accept	Accept
SE-054	12.131	0.003	2.578	0.007	0.528	1.772	0.007	1:1.11	Reject	Accept	Reject
SE-055	12.126	0.002	2.549	0.013	0.529	1.796	0.013	1:1.11	Reject	Accept	Reject
SE-056	12.135	0.003	2.570	0.012	0.529	1.779	0.012	1:1.11	Reject	Accept	Reject
SE-057	12.129	0.003	2.579	0.007	0.529	1.775	0.007	1:1.11	Accept	Accept	Accept
SE-058	12.136	0.002	2.563	0.026	0.528	1.781	0.026	1:1.11	Accept	Accept	Accept
SE-059	12.128	0.001	2.541	0.016	0.528	1.800	0.016	1:1.12	Accept	Accept	Accept
SE-060	12.135	0.004	2.552	0.011	0.528	1.790	0.011	1:1.11	Accept	Accept	Accept
SE-061	12.138	0.002	2.544	0.015	0.527	1.792	0.015	1:1.12	Reject	Accept	Reject
SE-062	12.135	0.003	2.560	0.007	0.527	1.778	0.007	1:1.11	Reject	Accept	Reject
SE-063	12.139	0.002	2.588	0.016	0.528	1.765	0.016	1:1.10	Reject	Accept	Reject
SE-064	12.137	0.001	2.524	0.005	0.527	1.805	0.005	1:1.12	Accept	Accept	Accept
SE-065	12.124	0.001	2.545	0.015	0.528	1.796	0.015	1:1.12	Reject	Accept	Reject
SE-066	12.117	0.001	2.526	0.004	0.524	1.798	0.004	1:1.12	Accept	Accept	Accept
SE-067	12.158	0.001	2.591	0.006	0.528	1.754	0.006	1:1.10	Accept	Accept	Accept
SE-068	12.150	0.003	2.555	0.007	0.527	1.778	0.007	1:1.11	Accept	Accept	Accept
SE-069	12.153	0.001	2.533	0.001	0.527	1.794	0.001	1:1.12	Accept	Accept	Accept
SE-070	12.143	0.002	2.553	0.009	0.527	1.784	0.009	1:1.11	Reject	Accept	Reject
SE-071	12.137	0.002	2.537	0.012	0.526	1.793	0.012	1:1.12	Reject	Accept	Reject
SE-072	12.130	0.002	2.570	0.008	0.529	1.780	0.008	1:1.11	Reject	Accept	Reject
SE-073	12.136	0.002	2.543	0.005	0.529	1.799	0.005	1:1.12	Reject	Accept	Reject
SE-074	12.181	0.035	2.565	0.003	0.527	1.761	0.003	1:1.11	Reject	Accept	Reject
SE-075	12.123	0.005	2.541	0.011	0.528	1.800	0.011	1:1.12	Accept	Accept	Accept
SE-076	12.132	0.004	2.565	0.003	0.528	1.781	0.003	1:1.11	Reject	Accept	Reject
SE-077	12.141	0.002	2.558	0.020	0.529	1.787	0.020	1:1.11	Reject	Accept	Reject
SE-078	12.145	0.002	2.509	0.006	0.523	1.800	0.006	1:1.13	Accept	Accept	Accept
SE-079	12.154	0.000	2.543	0.011	0.529	1.791	0.011	1:1.12	Reject	Accept	Reject
SE-080	12.140	0.001	2.521	0.005	0.526	1.802	0.005	1:1.12	Reject	Accept	Reject
SE-081	12.180	0.002	2.587	0.006	0.524	1.738	0.006	1:1.10	Reject	Accept	Reject
SE-082	12.183	0.001	2.617	0.016	0.525	1.721	0.016	1:1.09	Reject	Accept	Reject

Sample ID	Dia. (mm)	σ-Dia. (mm)	Length (mm)	σ-Length (mm)	Weight (g)	ρ (g/cm³)	σ-ρ (g/cm³)	SA:V	Status (visual)	Status (ρ)	Status (final)
SE-083	12.205	0.003	2.578	0.011	0.526	1.743	0.011	1:1.10	Reject	Accept	Reject
SE-084	12.163	0.004	2.594	0.014	0.527	1.747	0.014	1:1.10	Reject	Accept	Reject
SE-085	12.188	0.002	2.604	0.024	0.525	1.728	0.024	1:1.10	Reject	Accept	Reject
SE-086	12.185	0.004	2.578	0.007	0.525	1.745	0.007	1:1.10	Accept	Accept	Accept
SE-087	12.203	0.003	2.575	0.003	0.525	1.744	0.003	1:1.10	Reject	Accept	Reject
SE-088	12.207	0.002	2.579	0.013	0.526	1.742	0.013	1:1.10	Accept	Accept	Accept
SE-089	12.189	0.003	2.607	0.010	0.525	1.726	0.010	1:1.10	Reject	Accept	Reject
SE-090	12.191	0.006	2.582	0.014	0.525	1.743	0.014	1:1.10	Accept	Accept	Accept
SE-091	12.188	0.002	2.566	0.012	0.525	1.753	0.012	1:1.11	Reject	Accept	Reject
SE-092	12.187	0.003	2.601	0.016	0.526	1.734	0.016	1:1.10	Reject	Accept	Reject
SE-093	12.203	0.001	2.585	0.015	0.527	1.742	0.015	1:1.10	Reject	Accept	Reject
SE-094	12.179	0.002	2.568	0.005	0.526	1.757	0.005	1:1.11	Accept	Accept	Accept
SE-095	12.175	0.001	2.577	0.010	0.526	1.754	0.010	1:1.10	Accept	Accept	Accept
SE-096	12.191	0.001	2.588	0.008	0.527	1.744	0.008	1:1.10	Reject	Accept	Reject
SE-097	12.211	0.004	2.596	0.013	0.524	1.722	0.013	1:1.10	Reject	Accept	Reject
SE-098	12.197	0.002	2.568	0.019	0.526	1.752	0.019	1:1.11	Accept	Accept	Accept
SE-099	12.199	0.002	2.555	0.008	0.526	1.762	0.008	1:1.11	Accept	Accept	Accept
SE-100	12.199	0.002	2.570	0.015	0.526	1.750	0.015	1:1.11	Accept	Accept	Accept
SE-101	12.169	0.001	2.593	0.017	0.527	1.746	0.017	1:1.10	Reject	Accept	Reject
SE-102	12.155	0.003	2.546	0.016	0.525	1.777	0.016	1:1.11	Accept	Accept	Accept
SE-103	12.173	0.001	2.585	0.016	0.528	1.754	0.016	1:1.10	Reject	Accept	Reject
SE-104	12.157	0.004	2.564	0.019	0.528	1.774	0.019	1:1.11	Reject	Accept	Reject
SE-105	12.171	0.000	2.563	0.004	0.528	1.769	0.004	1:1.11	Reject	Accept	Reject
SE-106	12.169	0.004	2.585	0.014	0.528	1.756	0.014	1:1.10	Reject	Accept	Reject
SE-107	12.120	0.006	2.627	0.023	0.527	1.740	0.023	1:1.09	Accept	Accept	Accept
SE-108	12.153	0.002	2.565	0.011	0.527	1.772	0.011	1:1.11	Accept	Accept	Accept
SE-109	12.133	0.004	2.557	0.012	0.527	1.784	0.012	1:1.11	Reject	Accept	Reject
SE-110	12.156	0.005	2.564	0.005	0.527	1.772	0.005	1:1.11	Reject	Accept	Reject
SE-111	12.139	0.002	2.615	0.010	0.527	1.741	0.010	1:1.09	Reject	Accept	Reject
SE-112	12.183	0.002	2.607	0.036	0.527	1.732	0.036	1:1.10	Reject	Accept	Reject
SE-113	12.192	0.006	2.594	0.027	0.527	1.740	0.027	1:1.10	Accept	Accept	Accept
SE-114	12.100	0.019	2.612	0.016	0.527	1.753	0.016	1:1.10	Accept	Accept	Accept
SE-115	12.201	0.003	2.621	0.017	0.526	1.716	0.017	1:1.09	Accept	Accept	Accept
SE-116	12.187	0.005	2.617	0.007	0.527	1.726	0.007	1:1.09	Accept	Accept	Accept
SE-117	12.169	0.004	2.579	0.017	0.526	1.754	0.017	1:1.10	Accept	Accept	Accept
SE-118	12.191	0.005	2.639	0.008	0.527	1.709	0.008	1:1.09	Accept	Reject	Reject
SE-119	12.162	0.007	2.611	0.010	0.527	1.737	0.010	1:1.09	Accept	Accept	Accept
SE-120	12.194	0.006	2.594	0.020	0.526	1.736	0.020	1:1.10	Reject	Accept	Reject
SE-121	12.169	0.003	2.603	0.004	0.528	1.744	0.004	1:1.10	Accept	Accept	Accept
SE-122	12.180	0.001	2.583	0.009	0.525	1.743	0.009	1:1.10	Accept	Accept	Accept
SE-123	12.130	0.003	2.578	0.011	0.528	1.772	0.011	1:1.11	Accept	Accept	Accept
SE-124	12.139	0.006	2.576	0.009	0.527	1.767	0.009	1:1.11	Reject	Accept	Reject
SE-125	12.160	0.004	2.557	0.012	0.528	1.778	0.012	1:1.11	Reject	Accept	Reject
SE-126	12.165	0.008	2.595	0.004	0.528	1.749	0.004	1:1.10	Reject	Accept	Reject

Sample ID	Dia. (mm)	σ-Dia. (mm)	Length (mm)	σ-Length (mm)	Weight (g)	ρ (g/cm³)	σ-ρ (g/cm³)	SA:V	Status (visual)	Status (ρ)	Status (final)
SE-127	12.084	0.019	2.626	0.007	0.526	1.747	0.007	1:1.09	Accept	Accept	Accept
SE-128	12.174	0.004	2.591	0.018	0.527	1.748	0.018	1:1.10	Accept	Accept	Accept
SE-129	12.175	0.004	2.612	0.016	0.528	1.735	0.016	1:1.09	Accept	Accept	Accept
SE-130	12.172	0.003	2.578	0.017	0.524	1.747	0.017	1:1.10	Accept	Accept	Accept
SE-131	12.171	0.005	2.618	0.009	0.527	1.729	0.009	1:1.09	Accept	Accept	Accept
SE-132	12.170	0.005	2.617	0.013	0.527	1.730	0.013	1:1.09	Reject	Accept	Reject
SE-133	12.169	0.005	2.613	0.005	0.527	1.735	0.005	1:1.09	Accept	Accept	Accept
SE-134	12.180	0.003	2.611	0.012	0.527	1.730	0.012	1:1.09	Reject	Accept	Reject
SE-135	12.167	0.005	2.588	0.006	0.527	1.753	0.006	1:1.10	Reject	Accept	Reject
SE-136	12.152	0.013	2.596	0.015	0.527	1.752	0.015	1:1.10	Accept	Accept	Accept
SE-137	12.160	0.003	2.584	0.008	0.527	1.756	0.008	1:1.10	Accept	Accept	Accept
SE-138	12.117	0.018	2.630	0.006	0.527	1.738	0.006	1:1.09	Reject	Accept	Reject
SE-139	12.159	0.005	2.595	0.015	0.527	1.749	0.015	1:1.10	Accept	Accept	Accept
SE-140	12.148	0.003	2.584	0.006	0.528	1.761	0.006	1:1.10	Accept	Accept	Accept
SE-141	12.140	0.001	2.617	0.008	0.529	1.747	0.006	1:1.09	Accept	Accept	Accept
SE-142	12.143	0.001	2.594	0.008	0.529	1.761	0.006	1:1.10	Accept	Accept	Accept
SE-143	12.136	0.001	2.579	0.009	0.529	1.773	0.006	1:1.11	Reject	Accept	Reject
SE-144	12.153	0.002	2.585	0.004	0.530	1.767	0.003	1:1.10	Reject	Accept	Reject
SE-145	12.137	0.001	2.654	0.011	0.530	1.725	0.007	1:1.08	Reject	Accept	Reject
SE-146	12.153	0.001	2.580	0.006	0.529	1.768	0.004	1:1.10	Accept	Accept	Accept
SE-147	12.148	0.002	2.568	0.016	0.530	1.781	0.011	1:1.11	Reject	Accept	Reject
SE-148	12.132	0.004	2.603	0.010	0.529	1.758	0.007	1:1.10	Reject	Accept	Reject
SE-149	12.086	0.010	2.599	0.010	0.530	1.778	0.010	1:1.10	Accept	Accept	Accept
SE-150	12.139	0.003	2.566	0.003	0.530	1.783	0.003	1:1.11	Accept	Accept	Accept
SE-151	12.157	0.002	2.564	0.007	0.529	1.776	0.005	1:1.11	Reject	Accept	Reject
SE-152	12.142	0.002	2.541	0.001	0.528	1.795	0.001	1:1.12	Reject	Accept	Reject
SE-153	12.152	0.001	2.603	0.001	0.528	1.748	0.001	1:1.10	Reject	Accept	Reject
SE-154	12.184	0.001	2.588	0.016	0.521	1.727	0.010	1:1.10	Accept	Accept	Accept
SE-155	12.159	0.002	2.563	0.004	0.528	1.775	0.003	1:1.11	Accept	Accept	Accept
SE-156	12.162	0.002	2.545	0.003	0.527	1.783	0.003	1:1.11	Accept	Accept	Accept
SE-157	12.164	0.003	2.589	0.001	0.527	1.752	0.003	1:1.10	Reject	Accept	Reject
SE-158	12.162	0.002	2.589	0.007	0.527	1.752	0.005	1:1.10	Reject	Accept	Reject
SE-159	12.156	0.003	2.580	0.001	0.528	1.763	0.002	1:1.10	Reject	Accept	Reject
SE-160	12.164	0.001	2.604	0.018	0.528	1.744	0.012	1:1.10	Reject	Accept	Reject
SE-161	12.155	0.003	2.579	0.006	0.528	1.763	0.005	1:1.10	Reject	Accept	Reject
SE-162	12.157	0.000	2.535	0.002	0.529	1.796	0.001	1:1.12	Accept	Accept	Accept
SE-163	12.151	0.004	2.581	0.005	0.526	1.758	0.005	1:1.10	Reject	Accept	Reject
SE-164	12.166	0.001	2.583	0.037	0.525	1.747	0.025	1:1.10	Reject	Accept	Reject
SE-165	12.163	0.001	2.529	0.002	0.525	1.787	0.002	1:1.12	Reject	Accept	Reject
SE-166	12.172	0.001	2.549	0.001	0.526	1.773	0.001	1:1.11	Reject	Accept	Reject
SE-167	12.164	0.001	2.559	0.007	0.526	1.767	0.005	1:1.11	Reject	Accept	Reject
SE-168	12.179	0.000	2.561	0.004	0.527	1.765	0.003	1:1.11	Reject	Accept	Reject
SE-169	12.164	0.002	2.535	0.003	0.527	1.788	0.003	1:1.12	Accept	Accept	Accept
SE-170	12.168	0.002	2.562	0.005	0.526	1.766	0.004	1:1.11	Accept	Accept	Accept

Sample ID	Dia. (mm)	σ-Dia. (mm)	Length (mm)	σ-Length (mm)	Weight (g)	ρ (g/cm³)	σ-ρ (g/cm³)	SA:V	Status (visual)	Status (ρ)	Status (final)
SE-171	12.169	0.001	2.565	0.002	0.526	1.764	0.001	1:1.11	Reject	Accept	Reject
SE-172	12.177	0.001	2.551	0.011	0.527	1.773	0.008	1:1.11	Accept	Accept	Accept
SE-173	12.157	0.003	2.593	0.002	0.526	1.748	0.003	1:1.10	Reject	Accept	Reject
SE-174	12.176	0.002	2.567	0.003	0.527	1.763	0.003	1:1.11	Accept	Accept	Accept
SE-175	12.169	0.003	2.536	0.001	0.527	1.787	0.002	1:1.12	Reject	Accept	Reject
SE-176	12.170	0.000	2.573	0.002	0.527	1.760	0.002	1:1.11	Reject	Accept	Reject
SE-177	12.172	0.002	2.568	0.001	0.527	1.762	0.002	1:1.11	Reject	Accept	Reject
SE-178	12.169	0.000	2.531	0.004	0.526	1.788	0.003	1:1.12	Accept	Accept	Accept
SE-179	12.171	0.004	2.596	0.004	0.527	1.746	0.004	1:1.10	Reject	Accept	Reject
SE-180	12.173	0.002	2.581	0.002	0.527	1.754	0.002	1:1.10	Reject	Accept	Reject
SE-181	12.202	0.001	2.615	0.002	0.523	1.709	0.001	1:1.09	Reject	Reject	Reject
SE-182	12.183	0.004	2.584	0.007	0.527	1.751	0.006	1:1.10	Accept	Accept	Accept
SE-183	12.179	0.005	2.571	0.004	0.528	1.761	0.005	1:1.11	Reject	Accept	Reject
SE-184	12.171	0.006	2.604	0.005	0.527	1.739	0.005	1:1.10	Accept	Accept	Accept
SE-185	12.183	0.002	2.589	0.002	0.527	1.748	0.002	1:1.10	Reject	Accept	Reject
SE-186	12.184	0.003	2.615	0.003	0.527	1.729	0.003	1:1.09	Accept	Accept	Accept
SE-187	12.191	0.001	2.576	0.000	0.528	1.757	0.001	1:1.10	Reject	Accept	Reject
SE-188	12.170	0.004	2.578	0.001	0.527	1.758	0.003	1:1.10	Accept	Accept	Accept
SE-189	12.177	0.004	2.607	0.002	0.527	1.735	0.003	1:1.10	Reject	Accept	Reject
SE-190	12.180	0.001	2.567	0.006	0.527	1.761	0.004	1:1.11	Reject	Accept	Reject
SE-191	12.178	0.004	2.633	0.009	0.528	1.720	0.006	1:1.09	Reject	Accept	Reject
SE-192	12.193	0.000	2.588	0.002	0.527	1.745	0.001	1:1.10	Accept	Accept	Accept
SE-193	12.163	0.004	2.587	0.004	0.527	1.753	0.004	1:1.10	Reject	Accept	Reject
SE-194	12.190	0.002	2.589	0.000	0.528	1.746	0.001	1:1.10	Reject	Accept	Reject
SE-195	12.190	0.003	2.572	0.004	0.527	1.756	0.003	1:1.11	Reject	Accept	Reject
SE-196	12.177	0.001	2.589	0.003	0.527	1.748	0.002	1:1.10	Reject	Accept	Reject
SE-197	12.175	0.001	2.592	0.003	0.527	1.745	0.002	1:1.10	Reject	Accept	Reject
SE-198	12.173	0.005	2.604	0.004	0.526	1.736	0.005	1:1.10	Accept	Accept	Accept
SE-199	12.179	0.006	2.622	0.005	0.527	1.726	0.006	1:1.09	Reject	Accept	Reject
SE-200	12.167	0.000	2.641	0.004	0.528	1.718	0.002	1:1.09	Reject	Accept	Reject
SE-201	12.173	0.001	2.567	0.000	0.527	1.766	0.001	1:1.11	Reject	Accept	Reject
SE-202	12.172	0.002	2.605	0.002	0.527	1.739	0.002	1:1.10	Reject	Accept	Reject
SE-203	12.173	0.001	2.562	0.001	0.527	1.768	0.001	1:1.11	Reject	Accept	Reject
SE-204	12.160	0.002	2.567	0.004	0.528	1.770	0.004	1:1.11	Reject	Accept	Reject
SE-205	12.164	0.002	2.550	0.001	0.526	1.774	0.002	1:1.11	Accept	Accept	Accept
SE-206	12.164	0.002	2.597	0.001	0.528	1.750	0.002	1:1.10	Reject	Accept	Reject
SE-207	12.169	0.002	2.629	0.002	0.527	1.724	0.002	1:1.09	Reject	Accept	Reject
SE-208	12.163	0.002	2.564	0.007	0.527	1.769	0.005	1:1.11	Reject	Accept	Reject
SE-209	12.166	0.003	2.608	0.002	0.527	1.738	0.003	1:1.10	Reject	Accept	Reject
SE-210	12.184	0.006	2.587	0.011	0.526	1.743	0.008	1:1.10	Reject	Accept	Reject
SE-211	12.169	0.001	2.576	0.004	0.527	1.759	0.003	1:1.11	Reject	Accept	Reject
SE-212	12.176	0.004	2.625	0.001	0.527	1.723	0.003	1:1.09	Accept	Accept	Accept
SE-213	12.168	0.003	2.604	0.005	0.528	1.743	0.004	1:1.10	Reject	Accept	Reject
SE-214	12.170	0.003	2.572	0.003	0.527	1.762	0.003	1:1.11	Accept	Accept	Accept

Sample ID	Dia. (mm)	σ-Dia. (mm)	Length (mm)	σ-Length (mm)	Weight (g)	ρ (g/cm³)	σ-ρ (g/cm³)	SA:V	Status (visual)	Status (ρ)	Status (final)
SE-215	12.159	0.000	2.551	0.002	0.528	1.782	0.002	1:1.11	Reject	Accept	Reject
SE-216	12.184	0.001	2.587	0.004	0.527	1.746	0.003	1:1.10	Reject	Accept	Reject
SE-217	12.159	0.003	2.592	0.004	0.528	1.754	0.003	1:1.10	Reject	Accept	Reject
SE-218	12.164	0.005	2.592	0.006	0.528	1.753	0.005	1:1.10	Reject	Accept	Reject
SE-219	12.167	0.002	2.558	0.007	0.528	1.774	0.005	1:1.11	Reject	Accept	Reject
SE-220	12.163	0.002	2.586	0.005	0.528	1.756	0.004	1:1.10	Reject	Accept	Reject
SE-221	12.178	0.002	2.572	0.001	0.527	1.759	0.001	1:1.11	Accept	Accept	Accept
SE-222	12.179	0.001	2.592	0.007	0.527	1.744	0.005	1:1.10	Reject	Accept	Reject
SE-223	12.169	0.000	2.602	0.006	0.527	1.742	0.004	1:1.10	Reject	Accept	Reject
SE-224	12.172	0.002	2.631	0.002	0.527	1.721	0.002	1:1.09	Reject	Accept	Reject
SE-225	12.174	0.005	2.598	0.004	0.526	1.741	0.004	1:1.10	Reject	Accept	Reject
SE-226	12.176	0.002	2.565	0.002	0.527	1.764	0.002	1:1.11	Reject	Accept	Reject
SE-227	12.186	0.002	2.581	0.004	0.528	1.752	0.003	1:1.10	Reject	Accept	Reject
SE-228	12.172	0.002	2.584	0.002	0.527	1.753	0.002	1:1.10	Accept	Accept	Accept
SE-229	12.186	0.003	2.586	0.016	0.527	1.748	0.011	1:1.10	Reject	Accept	Reject
SE-230	12.179	0.003	2.597	0.002	0.527	1.741	0.003	1:1.10	Accept	Accept	Accept
SE-231	12.170	0.002	2.577	0.000	0.527	1.759	0.001	1:1.10	Accept	Accept	Accept
SE-232	12.186	0.004	2.619	0.002	0.527	1.726	0.003	1:1.09	Reject	Accept	Reject
SE-233	12.177	0.001	2.574	0.004	0.527	1.759	0.003	1:1.11	Reject	Accept	Reject
SE-234	12.179	0.004	2.594	0.000	0.527	1.744	0.003	1:1.10	Reject	Accept	Reject
SE-235	12.166	0.004	2.595	0.001	0.527	1.746	0.003	1:1.10	Accept	Accept	Accept
SE-236	12.102	0.016	2.594	0.005	0.522	1.750	0.012	1:1.10	Reject	Accept	Reject
SE-237	12.179	0.004	2.574	0.001	0.527	1.758	0.003	1:1.11	Accept	Accept	Accept
SE-238	12.166	0.004	2.648	0.005	0.528	1.714	0.004	1:1.08	Accept	Accept	Accept
SE-239	12.167	0.002	2.579	0.005	0.526	1.755	0.004	1:1.10	Accept	Accept	Accept
SE-240	12.166	0.003	2.565	0.007	0.526	1.765	0.005	1:1.11	Accept	Accept	Accept
SE-241	12.182	0.005	2.574	0.002	0.527	1.757	0.004	1:1.11	Accept	Accept	Accept
SE-242	12.171	0.004	2.574	0.005	0.527	1.761	0.004	1:1.11	Reject	Accept	Reject
SE-243	12.170	0.002	2.591	0.005	0.528	1.752	0.004	1:1.10	Reject	Accept	Reject
SE-244	12.172	0.002	2.623	0.001	0.528	1.729	0.001	1:1.09	Accept	Accept	Accept
SE-245	12.199	0.002	2.639	0.002	0.528	1.711	0.002	1:1.09	Reject	Reject	Reject
SE-246	12.177	0.000	2.577	0.003	0.528	1.759	0.002	1:1.10	Reject	Accept	Reject
SE-247	12.166	0.004	2.582	0.006	0.527	1.756	0.005	1:1.10	Reject	Accept	Reject
SE-248	12.182	0.001	2.610	0.003	0.527	1.734	0.002	1:1.09	Reject	Accept	Reject
SE-249	12.172	0.001	2.608	0.000	0.527	1.736	0.001	1:1.10	Reject	Accept	Reject
SE-250	12.191	0.002	2.609	0.004	0.527	1.732	0.003	1:1.09	Reject	Accept	Reject
SE-251	12.194	0.002	2.614	0.001	0.527	1.726	0.001	1:1.09	Reject	Accept	Reject
SE-252	12.167	0.001	2.603	0.000	0.528	1.743	0.001	1:1.10	Reject	Accept	Reject
SE-253	12.163	0.002	2.587	0.000	0.528	1.756	0.002	1:1.10	Reject	Accept	Reject
SE-254	12.184	0.002	2.681	0.007	0.527	1.687	0.005	1:1.07	Reject	Reject	Reject
SE-255	12.188	0.001	2.597	0.000	0.527	1.739	0.001	1:1.10	Reject	Accept	Reject
SE-256	12.171	0.003	2.588	0.002	0.527	1.750	0.003	1:1.10	Accept	Accept	Accept
SE-257	12.167	0.002	2.580	0.001	0.527	1.756	0.002	1:1.10	Reject	Accept	Reject
SE-258*	------	------	------	------	------	------	------	------		Reject	Reject

Sample ID	Dia. (mm)	σ-Dia. (mm)	Length (mm)	σ-Length (mm)	Weight (g)	ρ (g/cm³)	σ-ρ (g/cm³)	SA:V	Status (visual)	Status (ρ)	Status (final)
SE-259*	------	------	------	------	------	------	------	------		Reject	Reject
SE-260*	------	------	------	------	------	------	------	------		Reject	Reject
SE-261*	------	------	------	------	------	------	------	------		Reject	Reject
SE-262*	------	------	------	------	------	------	------	------		Reject	Reject
SE-263*	------	------	------	------	------	------	------	------		Reject	Reject
SE-264*	------	------	------	------	------	------	------	------		Reject	Reject
SE-265*	------	------	------	------	------	------	------	------		Reject	Reject
SE-266*	------	------	------	------	------	------	------	------		Reject	Reject
SE-267*	------	------	------	------	------	------	------	------		Reject	Reject
SE-268*	------	------	------	------	------	------	------	------		Reject	Reject
SE-269*	------	------	------	------	------	------	------	------		Reject	Reject
SE-270*	------	------	------	------	------	------	------	------		Reject	Reject
SE-271	12.176	0.004	2.644	0.005	0.526	1.709	0.004	1:1.08	Reject	Reject	Reject
SE-272	12.193	0.003	2.585	0.001	0.527	1.745	0.002	1:1.10	Accept	Accept	Accept
SE-273	12.171	0.000	2.546	0.001	0.528	1.781	0.001	1:1.11	Accept	Accept	Accept
SE-274	12.180	0.001	2.574	0.004	0.528	1.759	0.003	1:1.11	Reject	Accept	Reject
SE-275	12.190	0.003	2.627	0.001	0.526	1.716	0.002	1:1.09	Accept	Accept	Accept
SE-276	12.163	0.005	2.590	0.006	0.526	1.749	0.006	1:1.10	Reject	Accept	Reject
SE-277	12.167	0.002	2.591	0.001	0.527	1.750	0.002	1:1.10	Reject	Accept	Reject
SE-278	12.185	0.002	2.573	0.001	0.527	1.757	0.002	1:1.11	Reject	Accept	Reject
SE-279	12.176	0.004	2.595	0.002	0.527	1.743	0.003	1:1.10	Reject	Accept	Reject
SE-280	12.181	0.001	2.604	0.002	0.527	1.738	0.001	1:1.10	Reject	Accept	Reject
SE-281	12.196	0.001	2.604	0.000	0.527	1.733	0.001	1:1.10	Reject	Accept	Reject
SE-282	12.178	0.002	2.561	0.001	0.525	1.760	0.002	1:1.11	Accept	Accept	Accept
SE-283	12.180	0.004	2.595	0.003	0.527	1.742	0.004	1:1.10	Accept	Accept	Accept
SE-284	12.184	0.003	2.603	0.000	0.528	1.741	0.002	1:1.10	Accept	Accept	Accept
SE-285	12.173	0.004	2.580	0.005	0.529	1.760	0.004	1:1.10	Reject	Accept	Reject
SE-286	12.159	0.001	2.583	0.000	0.528	1.759	0.001	1:1.10	Reject	Accept	Reject
SE-287	12.094	0.015	2.593	0.013	0.528	1.772	0.014	1:1.10	Reject	Accept	Reject
SE-288	12.178	0.002	2.625	0.001	0.528	1.725	0.002	1:1.09	Accept	Accept	Accept
SE-289	12.180	0.003	2.610	0.001	0.526	1.731	0.002	1:1.09	Reject	Accept	Reject
SE-290	12.182	0.004	2.607	0.004	0.527	1.735	0.004	1:1.10	Reject	Accept	Reject
SE-291	12.160	0.003	2.605	0.011	0.528	1.744	0.008	1:1.10	Reject	Accept	Reject
SE-292	12.159	0.003	2.551	0.002	0.528	1.782	0.003	1:1.11	Accept	Accept	Accept
SE-293	12.165	0.003	2.555	0.002	0.528	1.777	0.003	1:1.11	Reject	Accept	Reject
SE-294	12.103	0.018	2.596	0.024	0.527	1.765	0.021	1:1.10	Accept	Accept	Accept
SE-295	12.213	0.000	2.556	0.001	0.527	1.761	0.001	1:1.11	Accept	Accept	Accept
SE-296	12.195	0.001	2.596	0.007	0.527	1.739	0.005	1:1.10	Reject	Accept	Reject
SE-297	12.188	0.006	2.569	0.001	0.527	1.760	0.004	1:1.11	Accept	Accept	Accept
SE-298	12.188	0.004	2.575	0.004	0.527	1.754	0.004	1:1.10	Reject	Accept	Reject
SE-299	12.168	0.001	2.601	0.001	0.527	1.742	0.001	1:1.10	Reject	Accept	Reject
SE-300	12.176	0.001	2.590	0.004	0.528	1.750	0.003	1:1.10	Accept	Accept	Accept

*SE-258–SE-270 were dropped after final heat treatment and therefore rejected.
^weight and density are reported for predrilled samples

APPENDIX B. INDIVIDUAL MEASUREMENTS AND TEST CONDITIONS FOR EMPIRICAL HIGH-TEMPERATURE OXIDATION TESTING

Table B-1. Results from empirical high-temperature oxidation testing showing weight loss for test conditions: 1,200–1,500 °C and 10–48 kPa

Temp.	P_{H2O} (kPa)	Exposure time (s)	Sample ID	Pre-oxidation weight (g)	Post-oxidation weight (g)	Weight loss (g)	Normalized weight loss	Residual oxygen weight loss	Adjusted oxidation weight loss
1200 °C	10	1800	SE-002	0.5185	0.4901	0.0284	5.47E-02	2.06E-02	3.42E-02
		3600	SE-020	0.5183	0.4654	0.0529	1.02E-01	2.99E-02	7.22E-02
		7200	SE-139	0.5175	0.3466	0.1708	3.30E-01	4.86E-02	2.82E-01
		14400	SE-141	0.5202	0.1477	0.3725	7.16E-01	8.60E-02	6.30E-01
	20	900	SE-007	0.5190	0.5049	0.0140	2.70E-02	1.59E-02	1.11E-02
		1800	SE-030	0.5180	0.4921	0.0259	5.00E-02	2.06E-02	2.95E-02
		3600	SE-001	0.5191	0.4500	0.0691	1.33E-01	2.99E-02	1.03E-01
		7200	SE-018	0.5188	0.3474	0.1714	3.30E-01	4.86E-02	2.82E-01
		7200	SE-066	0.5149	0.2500	0.2649	5.14E-01	4.86E-02	4.66E-01
		7200	SE-035	0.5179	0.3384	0.1795	3.47E-01	4.86E-02	2.98E-01
		10800	SE-038	0.5188	0.1770	0.3418	6.59E-01	6.73E-02	5.92E-01
		10800	SE-090	0.5162	0.1062	0.4100	7.94E-01	6.73E-02	7.27E-01
		14400	SE-059	0.5194	0.0398	0.4796	9.23E-01	8.60E-02	8.37E-01
	30	1800	SE-107	0.5182	0.4297	0.0885	1.71E-01	2.06E-02	1.50E-01
		3600	SE-113	0.5178	0.2987	0.2191	4.23E-01	2.99E-02	3.93E-01
		5400	SE-137	0.5181	0.1874	0.3307	6.38E-01	3.93E-02	5.99E-01
		7200	SE-114	0.5174	0.0990	0.4184	8.09E-01	4.86E-02	7.60E-01
	48	1800	SE-295	0.5192	0.4471	0.0721	1.39E-01	2.06E-02	1.18E-01
		3600	SE-297	0.5192	0.3351	0.1841	3.55E-01	2.99E-02	3.25E-01
		4500	SE-300	0.5192	0.2406	0.2786	5.37E-01	3.46E-02	5.02E-01
		3600	SE-198	0.5174	0.3096	0.2078	4.02E-01	2.99E-02	3.72E-01
		1800	SE-212	0.5181	0.4061	0.1120	2.16E-01	2.06E-02	1.96E-01
		5400	SE-228	0.5184	0.1741	0.3443	6.64E-01	3.93E-02	6.25E-01
		7200	SE-282	0.5164	0.0534	0.4630	8.97E-01	4.86E-02	8.48E-01
	------	1800	SE-039	0.5188	0.5099	0.0089	1.72E-02	------	------
		3600	SE-058	0.5190	0.5010	0.0181	3.48E-02	------	------
		7200	SE-067	0.5194	0.4949	0.0245	4.72E-02	------	------
		14400	SE-102	0.5163	0.4719	0.0444	8.60E-02	------	------
1300 °C	10	1800	SE-010	0.5196	0.4589	0.0607	1.17E-01	1.19E-02	1.05E-01
		3600	SE-032	0.5176	0.3918	0.1258	2.43E-01	1.84E-02	2.25E-01

Temp.	P_{H2O} (kPa)	Exposure time (s)	Sample ID	Pre-oxidation weight (g)	Post-oxidation weight (g)	Weight loss (g)	Normalized weight loss	Residual oxygen weight loss	Adjusted oxidation weight loss
		7200	SE-040	0.5169	0.2184	0.2984	5.77E-01	3.16E-02	5.46E-01
		9000	SE-142	0.5197	0.1534	0.3663	7.05E-01	3.81E-02	6.67E-01
	20	900	SE-149	0.5209	0.4874	0.0335	6.43E-02	8.60E-03	5.57E-02
		1800	SE-078	0.5144	0.4461	0.0682	1.33E-01	1.19E-02	1.21E-01
		3600	SE-133	0.5181	0.3236	0.1945	3.75E-01	1.84E-02	3.57E-01
		5400	SE-098	0.5166	0.2053	0.3112	6.02E-01	2.50E-02	5.77E-01
		5400	SE-057	0.5199	0.1546	0.3653	7.03E-01	2.50E-02	6.78E-01
		5400	SE-095	0.5173	0.1209	0.3964	7.66E-01	2.50E-02	7.41E-01
		7200	SE-130	0.5150	0.0433	0.4717	9.16E-01	3.16E-02	8.84E-01
		7200	SE-012	0.5177	0.0543	0.4634	8.95E-01	3.16E-02	8.64E-01
	30	1800	SE-214	0.5189	0.3833	0.1356	2.61E-01	1.19E-02	2.49E-01
		3600	SE-205	0.5173	0.1513	0.3660	7.08E-01	1.84E-02	6.89E-01
		5400	SE-230	0.5186	0.0197	0.4990	9.62E-01	2.50E-02	9.37E-01
		4500	SE-231	0.5191	0.0651	0.4540	8.75E-01	2.17E-02	8.53E-01
		2700	SE-235	0.5183	0.2416	0.2767	5.34E-01	1.52E-02	5.19E-01
	------	1800	SE-119	0.5176	0.5118	0.0058	1.12E-02	------	------
		3600	SE-136	0.5182	0.5081	0.0101	1.95E-02	------	------
		7200	SE-140	0.5180	0.5018	0.0162	3.12E-02	------	------
1400 °C	10	1800	SE-086	0.5157	0.3723	0.1435	2.78E-01	1.84E-02	2.60E-01
		2700	SE-023	0.5189	0.3217	0.1972	3.80E-01	2.23E-02	3.58E-01
		3600	SE-123	0.5187	0.2192	0.2996	5.78E-01	2.61E-02	5.51E-01
		5400	SE-122	0.5180	0.1355	0.3825	7.38E-01	3.38E-02	7.05E-01
		7200	SE-121	0.5190	0.0090	0.5099	9.83E-01	4.15E-02	9.41E-01
	20	900	SE-127	0.5167	0.4353	0.0814	1.58E-01	1.46E-02	1.43E-01
		1800	SE-146	0.5200	0.3645	0.1556	2.99E-01	1.84E-02	2.81E-01
		2700	SE-131	0.5176	0.2486	0.2690	5.20E-01	2.23E-02	4.97E-01
		3600	SE-128	0.5181	0.1621	0.3560	6.87E-01	2.61E-02	6.61E-01
		3600	SE-064	0.5183	0.1326	0.3858	7.44E-01	2.61E-02	7.18E-01
		3600	SE-099	0.5169	0.0698	0.4472	8.65E-01	2.61E-02	8.39E-01
		5400	SE-075	0.5191	0.0322	0.4869	9.38E-01	3.38E-02	9.04E-01
	30	1800	SE-238	0.5194	0.1855	0.3339	6.43E-01	1.84E-02	6.24E-01
		2700	SE-237	0.5191	0.0345	0.4846	9.33E-01	2.23E-02	9.11E-01
		900	SE-239	0.5178	0.4151	0.1027	1.98E-01	1.46E-02	1.84E-01
		2250	SE-241	0.5188	0.1514	0.3674	7.08E-01	2.04E-02	6.88E-01
		2700	SE-244	0.5194	0.0658	0.4536	8.73E-01	2.23E-02	8.51E-01
		2250	SE-256	0.5187	0.1650	0.3537	6.82E-01	2.04E-02	6.61E-01

Temp.	P_{H2O} (kPa)	Exposure time (s)	Sample ID	Pre-oxidation weight (g)	Post-oxidation weight (g)	Weight loss (g)	Normalized weight loss	Residual oxygen weight loss	Adjusted oxidation weight loss
	------	288	SE-069	0.5182	0.5143	0.0039	7.53E-03	------	------
		1800	SE-088	0.5166	0.5094	0.0072	1.39E-02	------	------
		3600	SE-094	0.5163	0.4949	0.0214	4.15E-02	------	------
		7200	SE-100	0.5163	0.4982	0.0181	3.51E-02	------	------
1500 °C	10	1800	SE-272	0.5183	0.3515	0.1668	3.22E-01	3.19E-02	2.90E-01
		3600	SE-283	0.5186	0.1873	0.3312	6.39E-01	5.03E-02	5.88E-01
		2700	SE-294	0.5187	0.2455	0.2732	5.27E-01	4.11E-02	4.86E-01
		2250	SE-288	0.5190	0.3031	0.2159	4.16E-01	3.65E-02	3.79E-01
		2700	SE-284	0.5200	0.2064	0.3136	6.03E-01	4.11E-02	5.62E-01
	------	3600	SE-273	0.5193	0.4925	0.0268	5.16E-02	------	------
		2700	SE-275	0.5177	0.4978	0.0199	3.84E-02	------	------
		1800	SE-240	0.5178	0.5006	0.0172	3.32E-02	------	------

APPENDIX C. INDIVIDUAL MEASUREMENTS AND TEST CONDITIONS FOR OXIDATION KINETICS EVALUATION

Table C-1. Results from oxidation kinetics evaluation testing showing test conditions and associated measured rate

Date	Sample ID	P_{H2O} (Pa)		P_{H2} (Pa)	Temp. (°C)	Rate (s^{-1})
		Target	Actual			
2/27/18	T-164	20	23	0	800	3.51E-09
2/25/18	T-162	20	40	0	800	0.00E+00
2/12/18	T-157	100	119	0	800	4.24E-10
3/22/18	T-170	100	122	0	800	6.21E-10
2/9/18	T-154	100	123	0	800	8.78E-10
2/14/18	T-155	200	222	0	800	4.22E-10
2/16/18	T-160	200	240	0	800	1.37E-10
3/5/18	T-169	300	293	0	800	1.13E-09
3/7/18	T-165	300	331	0	800	1.65E-10
2/22/18	T-161	500	480	0	800	1.51E-09
2/19/18	T-156	500	507	0	800	9.66E-10
2/27/18	T-164	20	24	0	850	3.69E-09
2/25/18	T-162	20	34	0	850	8.34E-10
2/12/18	T-157	100	122	0	850	1.08E-09
3/22/18	T-170	100	124	0	850	1.52E-09
2/9/18	T-154	100	154	0	850	3.35E-09
2/14/18	T-155	200	224	0	850	1.30E-09
2/16/18	T-160	200	258	0	850	5.61E-10
3/5/18	T-169	300	328	0	850	2.84E-09
3/7/18	T-165	300	381	0	850	2.37E-09
2/22/18	T-161	500	543	0	850	2.89E-09
2/19/18	T-156	500	617	0	850	2.03E-09
2/27/18	T-164	20	24	0	900	4.89E-09
2/25/18	T-162	20	34	0	900	2.78E-09
3/22/18	T-170	100	121	0	900	3.08E-09
2/9/18	T-154	100	137	0	900	1.34E-08
2/12/18	T-157	100	144	0	900	3.97E-09
2/14/18	T-155	200	234	0	900	4.19E-09
2/16/18	T-160	200	243	0	900	7.18E-09
3/7/18	T-165	300	347	0	900	7.11E-09
3/5/18	T-169	300	385	0	900	8.32E-09
2/22/18	T-161	500	573	0	900	1.14E-08
2/19/18	T-156	500	614	0	900	1.07E-08
2/27/18	T-164	20	24	0	950	1.06E-08

Date	Sample ID	P_{H2O} (Pa)		P_{H2} (Pa)	Temp. (°C)	Rate (s^{-1})
		Target	Actual			
2/25/18	T-162	20	34	0	950	7.40E-09
3/22/18	T-170	100	127	0	950	2.24E-08
2/9/18	T-154	100	130	0	950	6.75E-08
2/12/18	T-157	100	139	0	950	2.13E-08
2/14/18	T-155	200	239	0	950	2.83E-08
2/16/18	T-160	200	249	0	950	4.47E-08
3/5/18	T-169	300	367	0	950	4.50E-08
3/7/18	T-165	300	446	0	950	4.95E-08
2/22/18	T-161	500	573	0	950	7.62E-08
2/19/18	T-156	500	617	0	950	8.64E-08
2/27/18	T-164	20	24	0	1000	2.44E-08
2/25/18	T-162	20	33	0	1000	2.10E-08
3/22/18	T-170	100	129	0	1000	7.85E-08
2/9/18	T-154	100	130	0	1000	2.51E-07
2/12/18	T-157	100	134	0	1000	9.06E-08
2/14/18	T-155	200	245	0	1000	1.06E-07
2/16/18	T-160	200	256	0	1000	1.72E-07
3/5/18	T-169	300	349	0	1000	1.54E-07
3/7/18	T-165	300	419	0	1000	1.84E-07
2/22/18	T-161	500	573	0	1000	2.64E-07
2/19/18	T-156	500	688	0	1000	2.80E-07
2/25/18	T-162	20	16	0	1050	3.58E-08
2/27/18	T-164	20	24	0	1050	5.47E-08
2/12/18	T-157	100	125	0	1050	2.07E-07
2/9/18	T-154	100	131	0	1050	4.89E-07
3/22/18	T-170	100	171	0	1050	2.31E-07
2/14/18	T-155	200	245	0	1050	2.67E-07
2/16/18	T-160	200	255	0	1050	4.13E-07
3/7/18	T-165	300	340	0	1050	4.04E-07
3/5/18	T-169	300	350	0	1050	3.68E-07
2/22/18	T-161	500	570	0	1050	6.45E-07
2/19/18	T-156	500	582	0	1050	6.31E-07
2/25/18	T-162	20	16	0	1100	8.14E-08
2/27/18	T-164	20	24	0	1100	1.22E-07
6/4/18	T-162-1	20	54	0	1100	2.17E-07
3/22/18	T-170	100	117	0	1100	4.13E-07
2/12/18	T-157	100	126	0	1100	4.67E-07
2/9/18	T-154	100	131	0	1100	9.66E-07
5/22/18	T-157-1	100	174	0	1100	7.17E-07

Date	Sample ID	P_{H2O} (Pa)		P_{H2} (Pa)	Temp. (°C)	Rate (s^{-1})
		Target	Actual			
5/24/18	T-155-1	200	227	0	1100	7.39E-07
2/14/18	T-155	200	242	0	1100	6.50E-07
2/16/18	T-160	200	256	0	1100	9.72E-07
5/29/18	T-169-1	300	304	0	1100	8.93E-07
3/7/18	T-165	300	340	0	1100	9.39E-07
5/30/18	T-156-1	500	417	0	1100	1.42E-06
3/5/18	T-169	300	460	0	1100	1.06E-06
2/22/18	T-161	500	572	0	1100	1.59E-06
2/19/18	T-156	500	611	0	1100	1.60E-06
2/19/18	T-156	20	67	0	1150	4.67E-07
2/19/18	T-156	100	118	0	1150	1.20E-06
3/22/18	T-170	100	129	0	1150	9.75E-07
2/19/18	T-156	200	217	0	1150	1.56E-06
2/19/18	T-156	300	294	0	1150	1.85E-06
2/19/18	T-156	500	433	0	1150	3.02E-06
3/22/18	T-170	20	66	0	1200	9.92E-07
3/22/18	T-170	100	121	0	1200	2.26E-06
3/22/18	T-170	100	130	0	1200	1.89E-06
3/22/18	T-170	200	219	0	1200	3.04E-06
3/22/18	T-170	300	296	0	1200	3.56E-06
3/22/18	T-170	500	434	0	1200	5.65E-06
4/19/18	T-175	20	62	20	800	0.00E+00
3/31/18	T-167	100	121	21	800	5.95E-10
3/27/18	T-172	100	191	21	800	9.75E-10
4/2/18	T-174	200	237	21	800	1.08E-09
4/4/18	T-168	300	323	20	800	4.53E-10
4/9/18	T-178	500	495	21	800	1.35E-09
4/30/18	T-182	100	128	85	800	4.90E-10
4/23/18	T-176	200	220	84	800	3.24E-09
5/2/18	T-184	300	316	84	800	9.87E-10
5/8/18	T-186	500	513	84	800	1.08E-09
4/19/18	T-175	20	34	20	850	0.00E+00
3/31/18	T-167	100	123	21	850	8.96E-10
3/27/18	T-172	100	141	21	850	1.07E-09
4/2/18	T-174	200	250	21	850	6.01E-10
4/4/18	T-168	300	325	20	850	8.57E-10
4/9/18	T-178	500	571	21	850	9.01E-10
4/30/18	T-182	100	128	85	850	6.27E-10
4/23/18	T-176	200	220	84	850	1.16E-09

Date	Sample ID	P_{H2O} (Pa)		P_{H2} (Pa)	Temp. (°C)	Rate (s^{-1})
		Target	Actual			
5/2/18	T-184	300	329	84	850	5.77E-10
5/8/18	T-186	500	571	84	850	8.75E-10
4/19/18	T-175	20	17	20	900	6.87E-10
3/31/18	T-167	100	124	21	900	1.09E-09
3/27/18	T-172	100	162	21	900	4.18E-09
4/2/18	T-174	200	257	21	900	2.12E-09
4/4/18	T-168	300	400	20	900	3.35E-09
4/9/18	T-178	500	581	21	900	5.69E-09
4/30/18	T-182	100	130	85	900	4.46E-10
4/23/18	T-176	200	226	84	900	1.94E-09
5/2/18	T-184	300	368	84	900	1.71E-09
5/8/18	T-186	500	571	84	900	2.99E-09
4/19/18	T-175	20	17	20	950	8.80E-10
3/31/18	T-167	100	124	21	950	4.69E-09
3/27/18	T-172	100	141	21	950	1.29E-08
4/2/18	T-174	200	261	21	950	1.40E-08
4/4/18	T-168	300	368	20	950	2.30E-08
4/9/18	T-178	500	568	21	950	3.89E-08
4/30/18	T-182	100	132	85	950	1.74E-09
4/23/18	T-176	200	244	84	950	5.32E-09
5/2/18	T-184	300	336	84	950	7.35E-09
5/8/18	T-186	500	572	84	950	1.54E-08
4/19/18	T-175	20	17	20	1000	8.72E-09
3/31/18	T-167	100	124	21	1000	2.29E-08
3/27/18	T-172	100	142	21	1000	4.48E-08
4/2/18	T-174	200	267	21	1000	9.37E-08
4/4/18	T-168	300	369	20	1000	1.46E-07
4/9/18	T-178	500	566	21	1000	1.95E-07
4/30/18	T-182	100	132	85	1000	9.32E-09
4/23/18	T-176	200	248	84	1000	3.07E-08
5/2/18	T-184	300	363	84	1000	5.06E-08
5/8/18	T-186	500	575	84	1000	1.21E-07
4/19/18	T-175	20	17	20	1050	2.13E-08
3/31/18	T-167	100	123	21	1050	9.66E-08
3/27/18	T-172	100	142	21	1050	1.28E-07
4/2/18	T-174	200	261	21	1050	2.59E-07
4/4/18	T-168	300	377	20	1050	3.90E-07
4/9/18	T-178	500	574	21	1050	5.03E-07
4/30/18	T-182	100	133	85	1050	4.45E-08

Date	Sample ID	P_{H2O} (Pa)		P_{H2} (Pa)	Temp. (°C)	Rate (s^{-1})
		Target	Actual			
4/23/18	T-176	200	255	84	1050	1.54E-07
5/2/18	T-184	300	380	84	1050	2.19E-07
5/8/18	T-186	500	576	84	1050	3.71E-07
4/19/18	T-175	20	17	20	1100	5.17E-08
3/31/18	T-167	100	133	21	1100	2.57E-07
3/27/18	T-172	100	140	21	1100	3.04E-07
4/2/18	T-174	200	252	21	1100	6.25E-07
4/4/18	T-168	300	364	20	1100	9.45E-07
4/9/18	T-178	500	535	21	1100	1.15E-06
4/30/18	T-182	100	133	85	1100	1.43E-07
4/23/18	T-176	200	255	84	1100	3.79E-07
5/2/18	T-184	300	384	84	1100	5.90E-07
5/8/18	T-186	500	564	84	1100	9.25E-07
4/19/18	T-175	20	17	20	1150	1.04E-07
3/31/18	T-167	100	129	21	1150	6.63E-07
3/27/18	T-172	100	133	21	1150	6.88E-07
4/2/18	T-174	200	251	21	1150	1.38E-06
4/4/18	T-168	300	426	20	1150	2.35E-06
4/9/18	T-178	500	484	21	1150	2.44E-06
4/30/18	T-182	100	133	85	1150	3.76E-07
4/23/18	T-176	200	258	84	1150	9.50E-07
5/2/18	T-184	300	397	84	1150	1.50E-06
5/8/18	T-186	500	574	85	1150	2.04E-06
4/19/18	T-175	20	17	20	1200	1.79E-07
3/31/18	T-167	100	130	21	1200	1.49E-06
3/27/18	T-172	100	134	21	1200	1.53E-06
4/2/18	T-174	200	251	21	1200	3.11E-06
4/4/18	T-168	300	387	20	1200	4.44E-06
4/9/18	T-178	500	484	21	1200	4.70E-06
4/30/18	T-182	100	133	85	1200	9.46E-07
4/23/18	T-176	200	262	84	1200	2.20E-06
5/2/18	T-184	300	357	84	1200	3.13E-06
5/8/18	T-186	500	576	84	1200	4.43E-06

APPENDIX D. SELECT OPTICAL MICROGRAPHS OF SAMPLES SUBJECTED TO CROSS SECTIONAL ANALYSIS

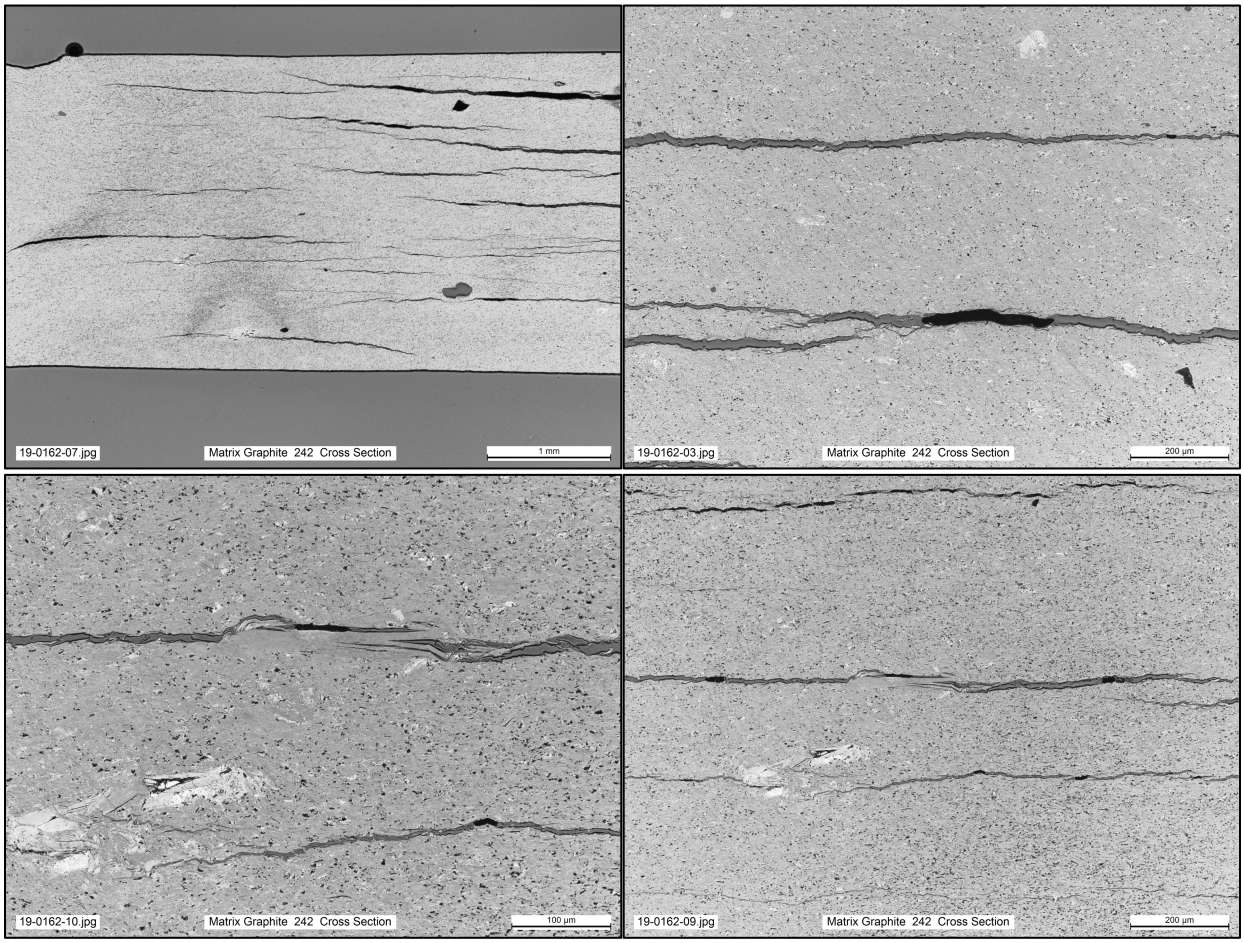

SE-242, As-fabricated

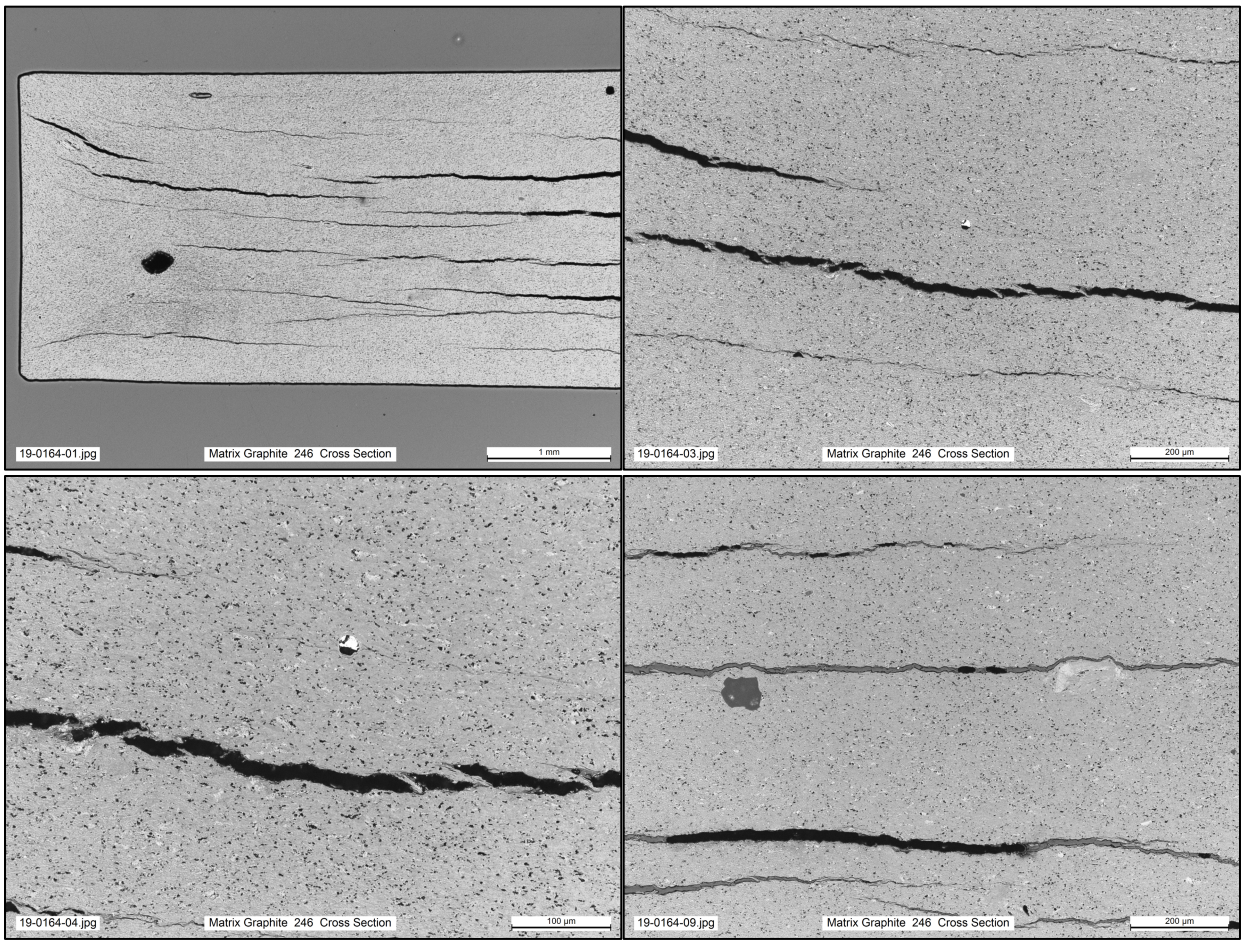

SE-246, As-fabricated

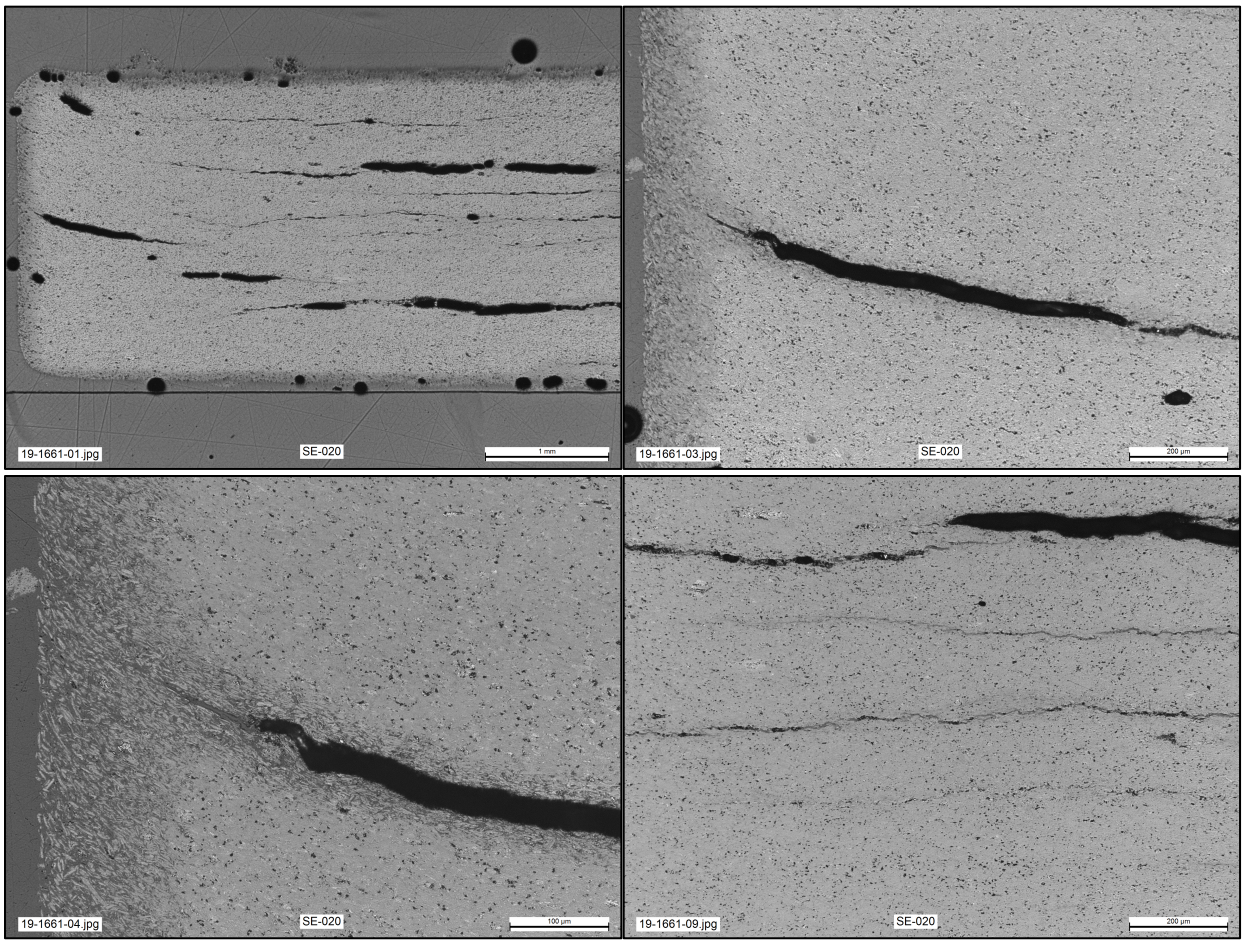

SE-020, 1,200 °C, 1 h, 10 kPa

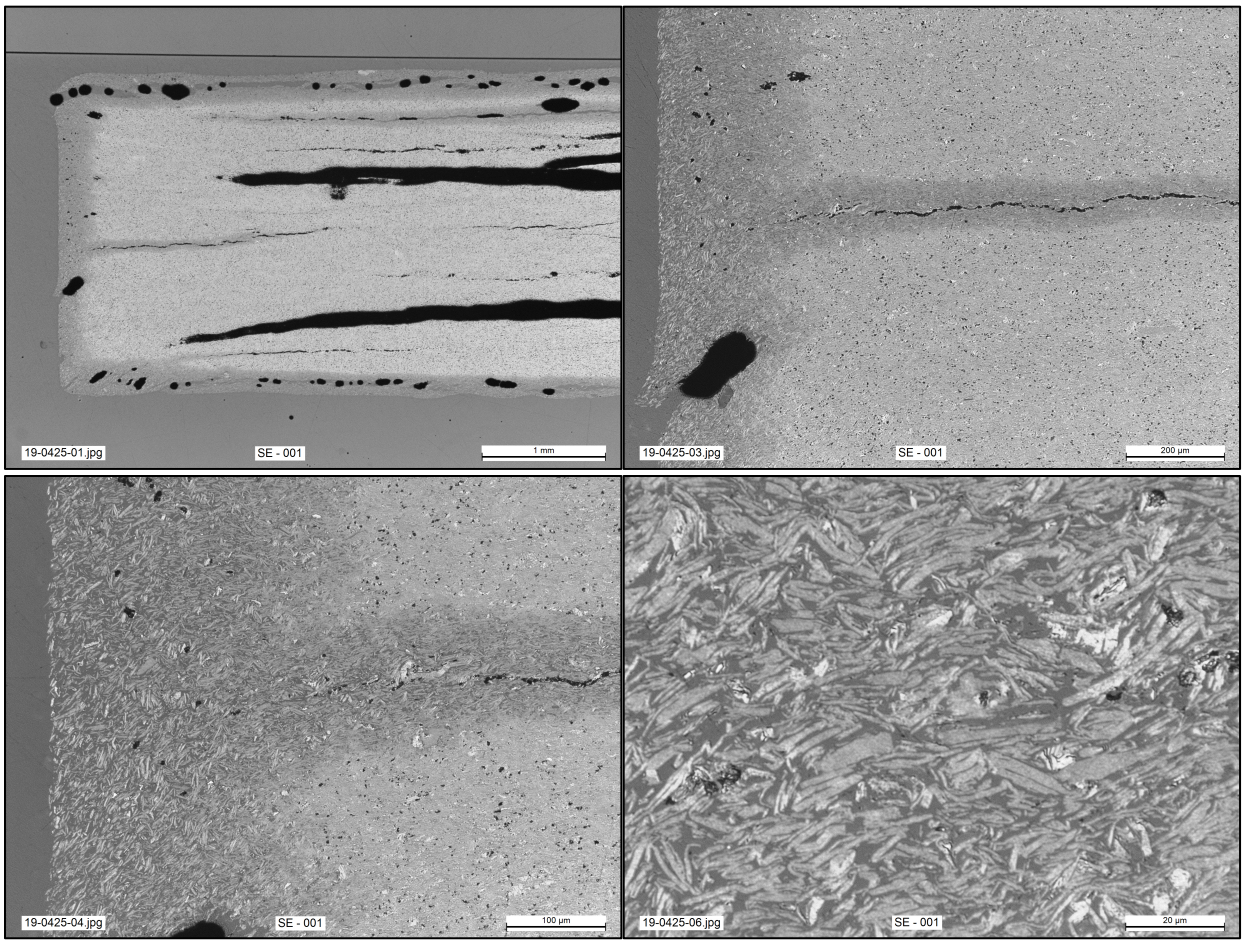

SE-001, 1,200 °C, 1 h, 20 kPa

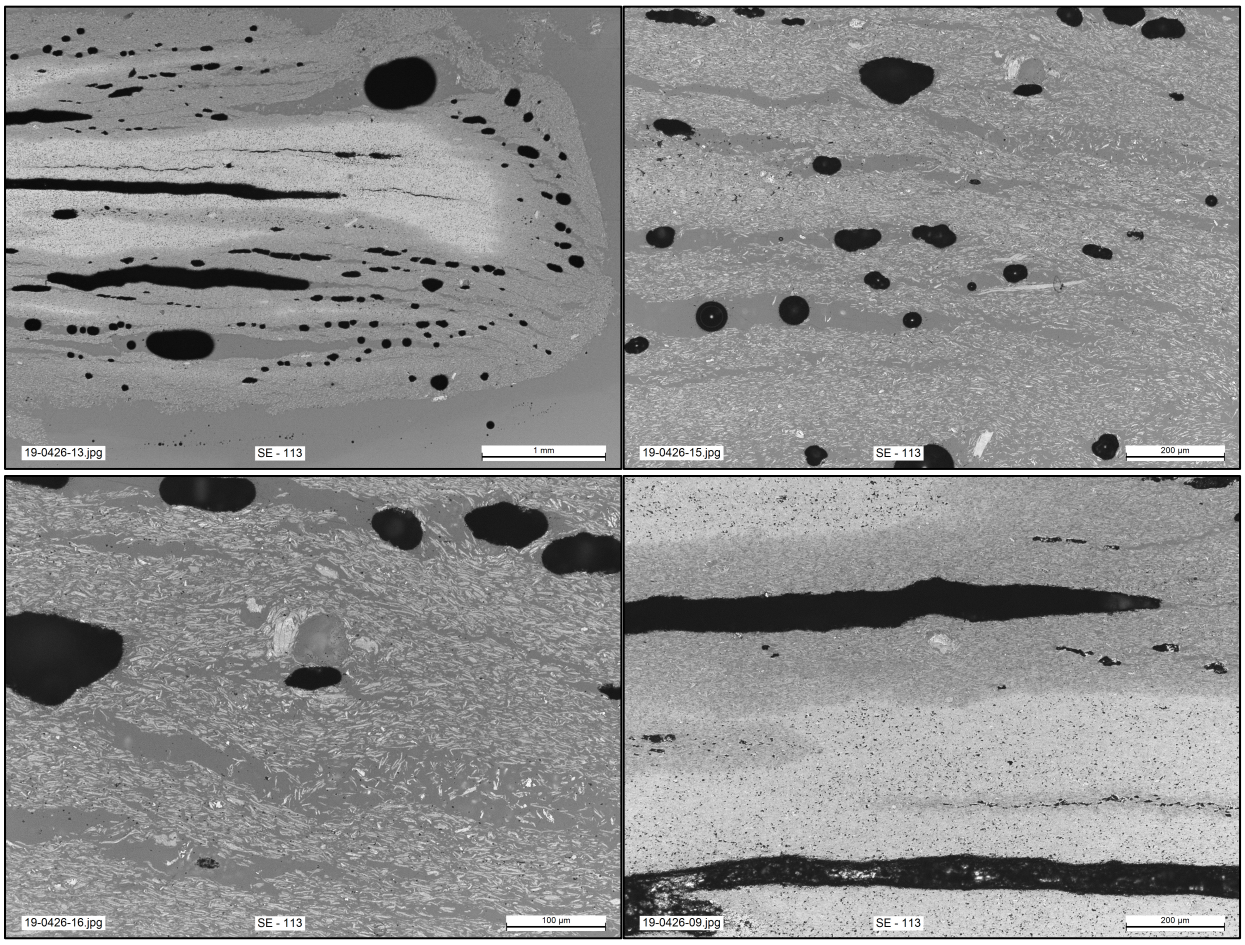

SE-113, 1,200 °C, 1 h, 30 kPa

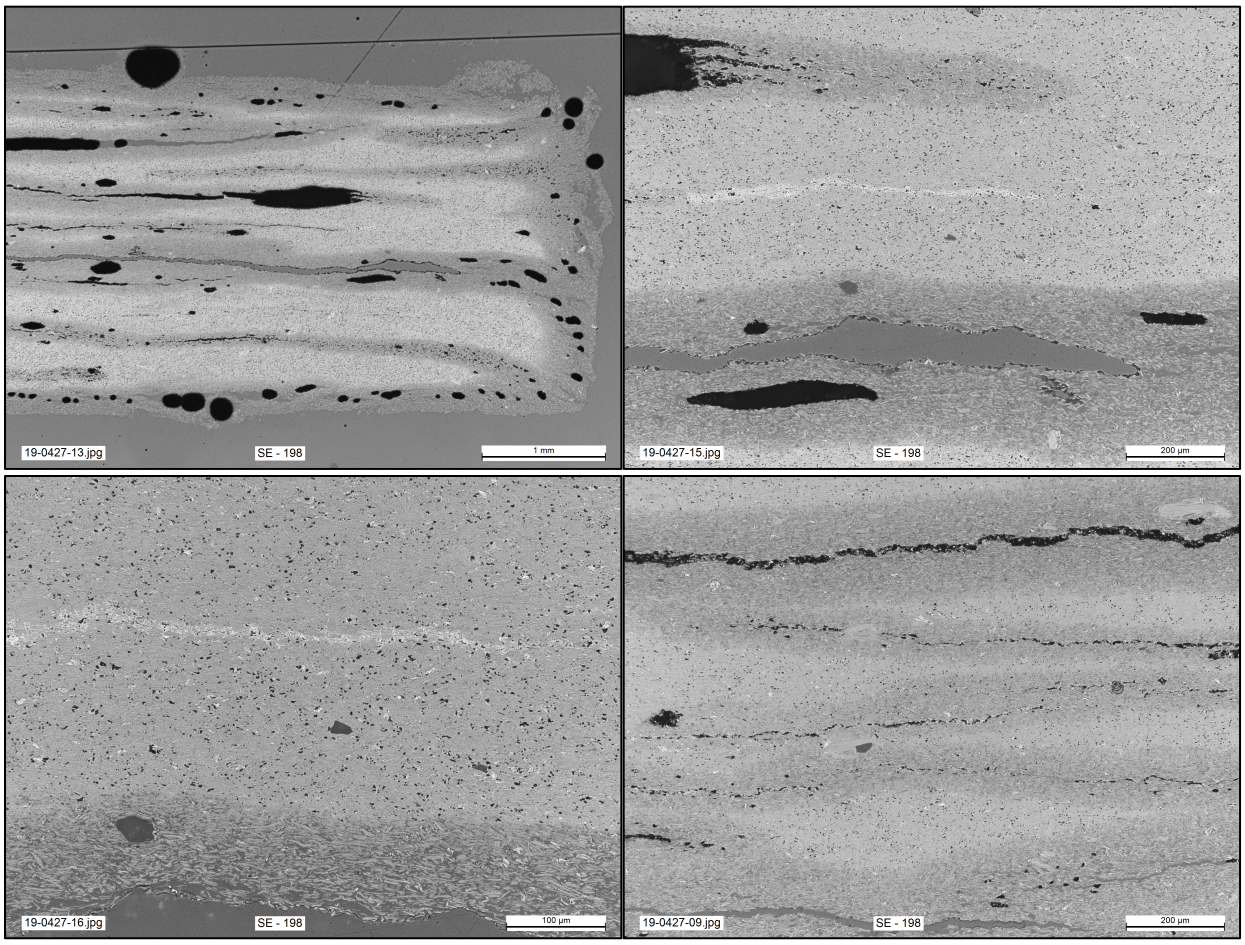

SE-198, 1,200 °C, 1 h, 48 kPa

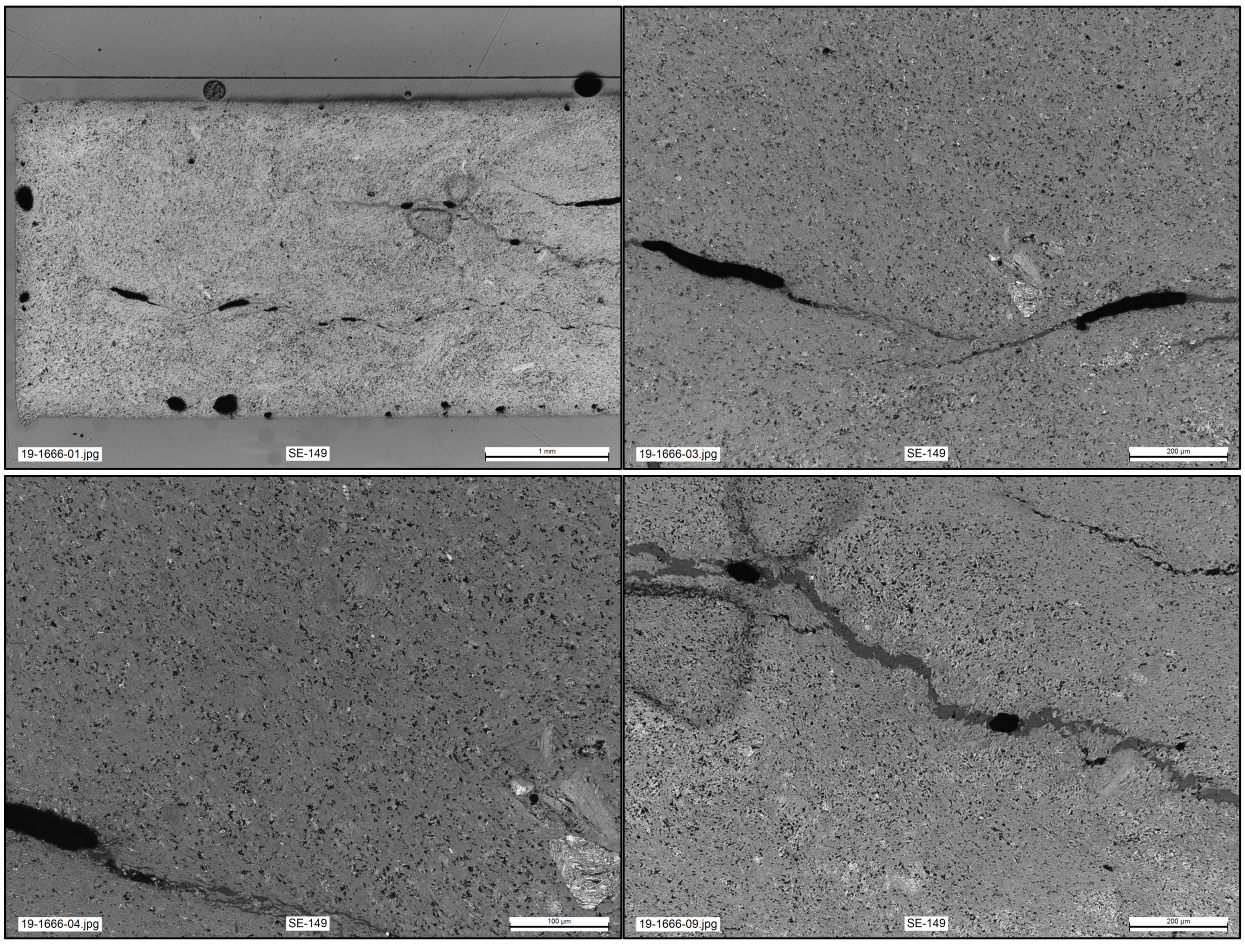

SE-149, 1,300 °C, 0.25 h, 20 kPa

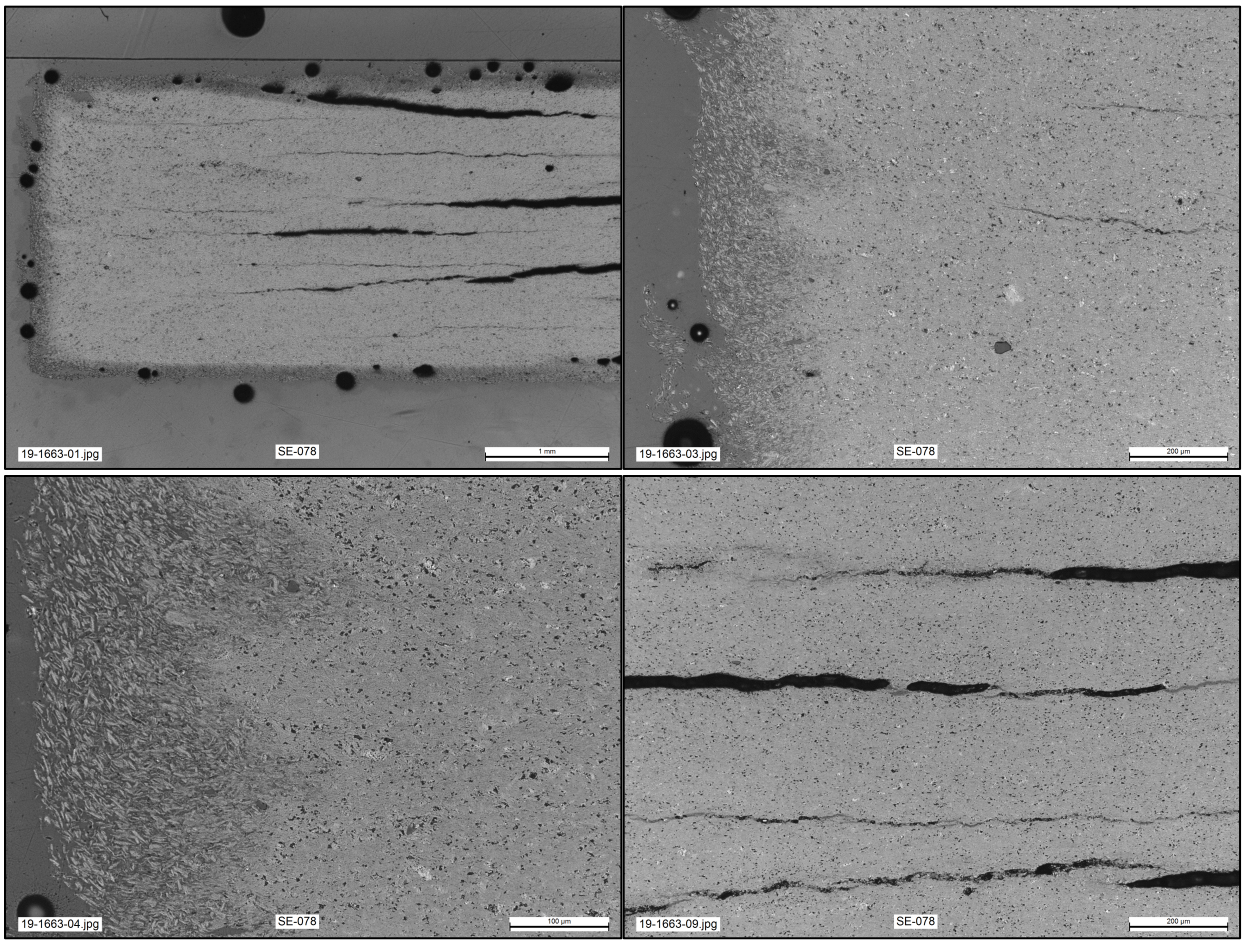

SE-078, 1,300 °C, 0.5 h, 20 kPa

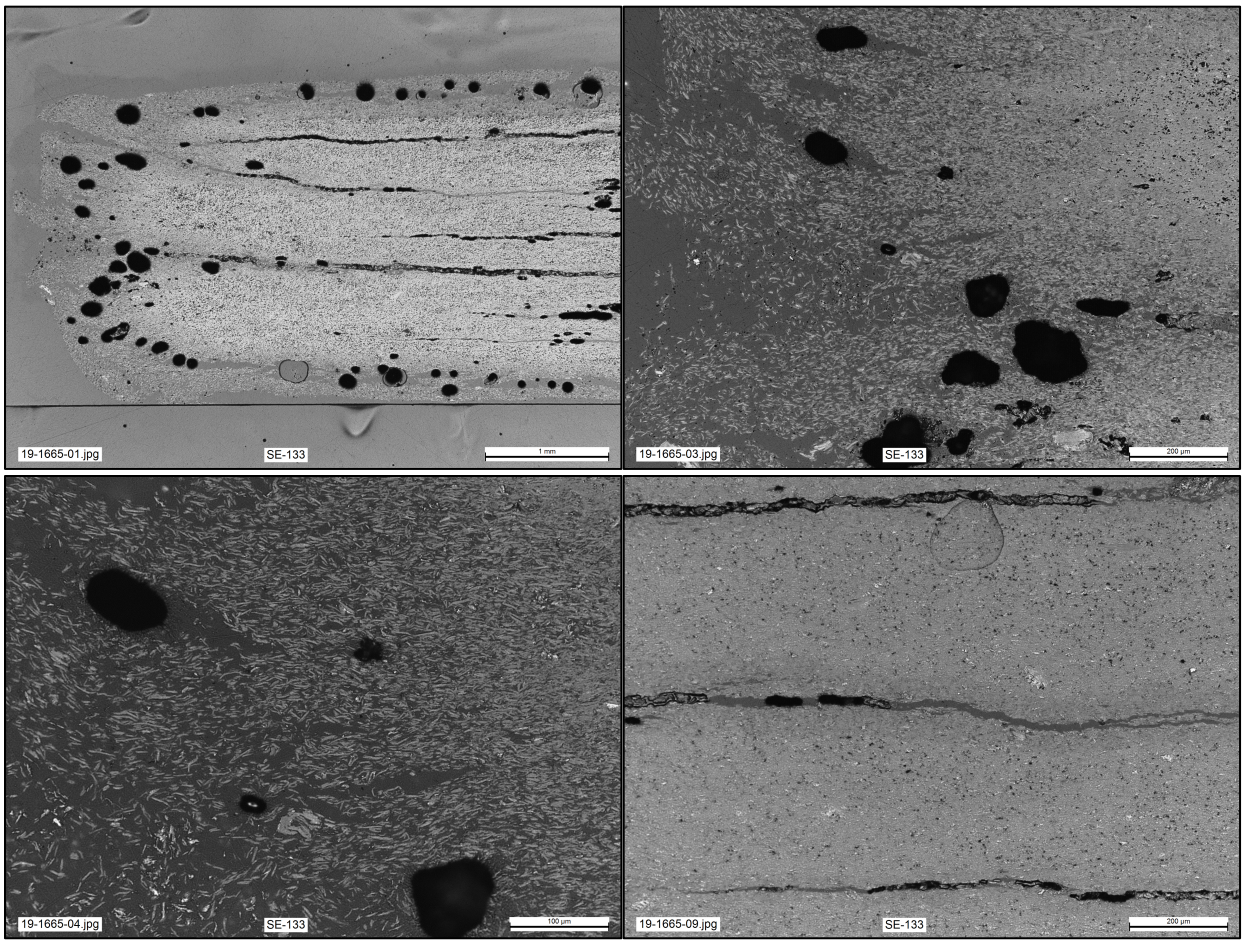

SE-133, 1,300 °C, 1 h, 20 kPa

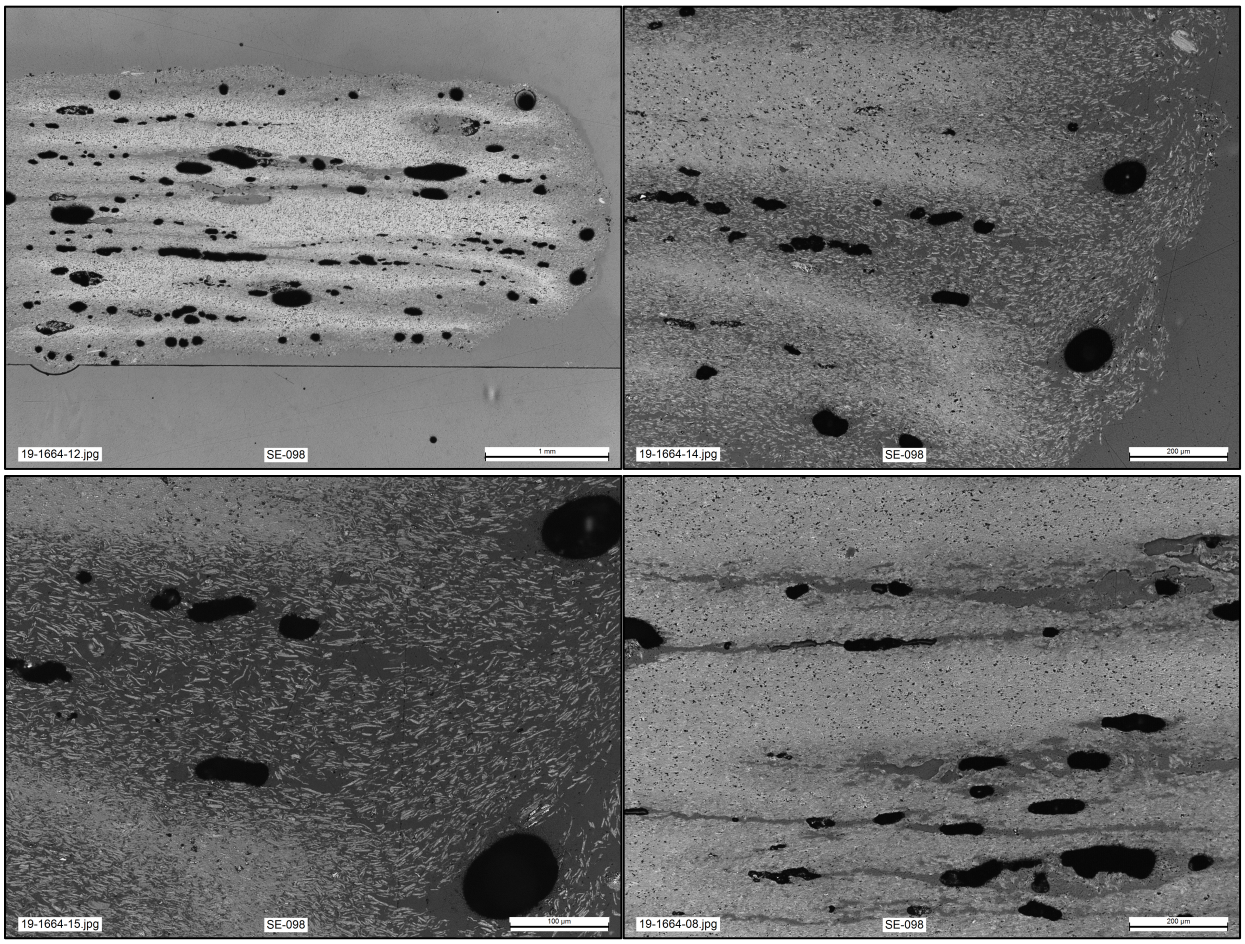

SE-098, 1,300 °C, 1.5 h, 20 kPa

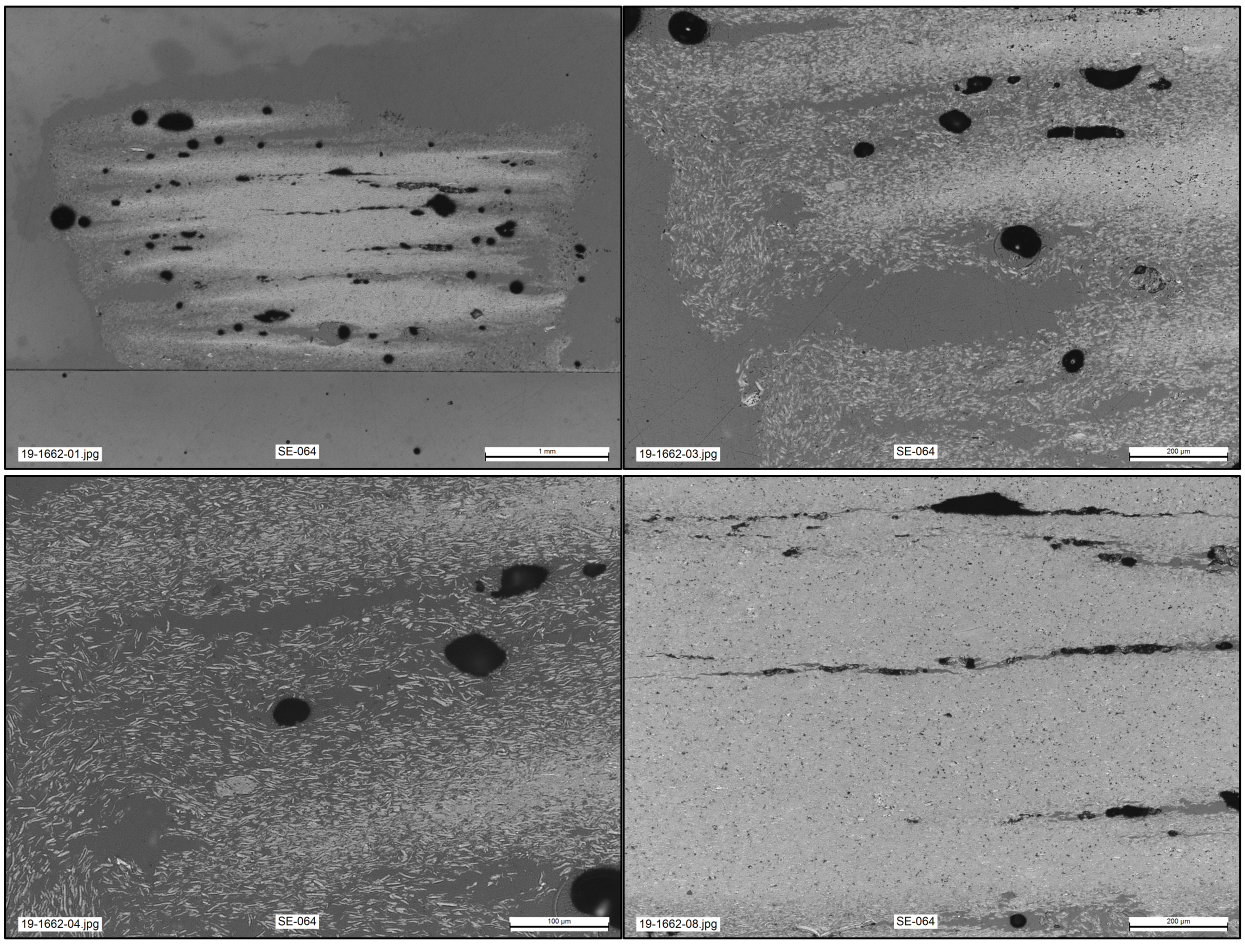

SE-064, 1,400 °C, 1 h, 20 kPa